General Disclaimer

One or more of the Following Statements may affect this Document

- This document has been reproduced from the best copy furnished by the organizational source. It is being released in the interest of making available as much information as possible.

- This document may contain data, which exceeds the sheet parameters. It was furnished in this condition by the organizational source and is the best copy available.

- This document may contain tone-on-tone or color graphs, charts and/or pictures, which have been reproduced in black and white.

- This document is paginated as submitted by the original source.

- Portions of this document are not fully legible due to the historical nature of some of the material. However, it is the best reproduction available from the original submission.

ORIENTATION DEPENDENCE OF
THE STRESS RUPTURE PROPERTIES
OF NICKEL-BASE SUPERALLOY SINGLE CRYSTALS

BY

REBECCA A. MACKAY AND RALPH D. MAIER

CASE WESTERN RESERVE UNIVERSITY

NOV 1982
RECEIVED
NASA STI FACILITY
ACCESS DEPT.

PREPARED FOR

NATIONAL AERONAUTICS AND SPACE ADMINISTRATION

MAY 1981

NASA LEWIS RESEARCH CENTER
GRANT NSG-3246

1. Report No. CR-165394	2. Government Accession No.	3. Recipient's Catalog No.
4. Title and Subtitle Orientation Dependence of the Stress Rupture Properties of Nickel-Base Superalloy Single Crystals		5. Report Date June 15, 1981
		6. Performing Organization Code
7. Author(s) Rebecca A. MacKay		8. Performing Organization Report No.
		10. Work Unit No.
9. Performing Organization Name and Address CaseWestern Reserve University Cleveland, Ohio 44106		11. Contract or Grant No. NSG-3246
		13. Type of Report and Period Covered Contractor Report 6/79-6/81
12. Sponsoring Agency Name and Address National Aeronautics and Space Administration Washington, D. C. 20546		14. Sponsoring Agency Code

15. Supplementary Notes

16. Abstract   The influence of orientation of the stress rupture behavior of Mar-M247 single crystals was studied. Stress rupture tests were performed at 724 MPa and 774°C where the effect of anisotropy is prominent.

The mechanical behavior of the single crystals was rationalized on the basis of the Schmid factors for the operative slip systems and the lattice rotations which the crystals underwent during deformation. The stress rupture lives were found to be greatly influenced by the lattice rotations required to produce intersecting slip, because steady-state creep does not begin until after the onset of intersecting slip. Crystals which required large rotations to become oriented for intersecting slip exhibited a large primary creep strain, a large effective stress level at the onset of steady-state creep, and consequently a short stress rupture life.

A unified analysis was attained for the stress rupture behavior of the Mar-M247 single crystals tested in this study at 774°C and that of the Mar-M200 single crystals tested in a prior study at 760°C. In this analysis, the standard [001]-[011]-[111] stereographic triangle was divided into several regions of crystallographic orientation which were rank ordered according to stress rupture life for this temperature regime. This plot indicates that those crystals having orientations within about 25° of the [001] exhibited significantly longer lives when their orientations were closer to the [001]-[011] boundary of the stereographic triangle than to the [001]-[111] boundary.

Therefore, the direction off the [001], as well as the number of degrees off the [001], has a major influence on the stress rupture lives of single crystals in this temperature regime. This finding has commercial significance because crystals with orientations near the [001] are utilized for most single crystal turbine blade applications. Hence, it may be appropriate to incorporate the effect of the direction off the [001] in pass/fail criteria employed to specify acceptable single crystal turbine blades.

17. Key Words (Suggested by Author(s)) Single crystals Nickel-base superalloy Stress rupture properties Mar-M247	18. Distribution Statement Unclassified, unlimited

19. Security Classif. (of this report) Unclassified	20. Security Classif. (of this page) Unclassified	21. No. of Pages 95	22. Price*

NASA-C-168 (Rev. 6-71)

ORIENTATION DEPENDENCE OF

THE STRESS RUPTURE PROPERTIES

OF NICKEL-BASE SUPERALLOY SINGLE CRYSTALS

by

REBECCA ANN MACKAY

Submitted in partial fulfillment of the requirements

for the Degree of Master of Science

Department of Metallurgy and Materials Science

CASE WESTERN RESERVE UNIVERSITY

May 1981

ORIENTATION DEPENDENCE OF
THE STRESS RUPTURE PROPERTIES
OF NICKEL-BASE SUPERALLOY SINGLE CRYSTALS

Abstract

The influence of orientation on the stress rupture behavior of twenty-three Mar-M247 single crystals was studied. Stress rupture tests were performed at 724 MPa and $774^{\circ}C$ where the effect of anisotropy is prominent.

The mechanical behavior of the single crystals was rationalized on the basis of the Schmid factors for the operative slip systems and the lattice rotations which the crystals underwent during deformation. The stress rupture lives at $774^{\circ}C$ were found to be greatly influenced by the lattice rotations required to produce intersecting slip, because steady-state creep does not begin until after the onset of intersecting slip. Crystals which required large rotations to become ori-

ented for intersecting slip exhibited a large primary creep strain, a large effective stress level at the onset of steady-state creep, and consequently a short stress rupture life. Conversely, crystals which required little or no rotations to become oriented for intersecting slip exhibited much longer stress rupture lives.

Based on a consideration of the lattice rotations, the Schmid factors, and the stress rupture data, a unified analysis was attained for the stress rupture behavior of the Mar-M247 single crystals tested in this study at $774^{\circ}C$ and that of the Mar-M200 single crystals tested in a prior study at $760^{\circ}C$. In this analysis, the standard [001] - [011] - [$\bar{1}$11] stereographic triangle was divided into several regions of crystallographic orientation which were rank ordered according to stress rupture life for this temperature regime. This plot indicates that the longest lives occurred for crystals having orientations near the [$\bar{1}$11]; long lives were exhibited by crystals having orientations near the [001]; and the shortest lives were exhibited by crystals oriented near the [011]. Those crystals having orientations within about 25° of the [001] exhibited significantly longer lives when their orientations were closer to the [001] - [011]

boundary of the stereographic triangle than to the [001] - [$\bar{1}$11] boundary.

Therefore, the direction off the [001], as well as the number of degrees off the [001], has a major influence on the stress rupture lives of single crystals in this temperature regime. This finding has commercial significance because crystals with orientations near the [001] are utilized for most single crystal turbine blade applications. Hence, it may be appropriate to incorporate the effect of the direction off the [001] in pass/fail criteria employed to specify acceptable single crystal turbine blades.

ACKNOWLEDGEMENTS

TABLE OF CONTENTS

LIST OF TABLES

LIST OF FIGURES

INTRODUCTION

Superalloy Development

The performance and efficiency of the aircraft gas
turbine engine improve with increasing operating tem-
perature. For this reason, considerable research has
been directed toward developing turbine blade and vane
materials capable of operating at increasingly higher
temperatures in the high pressure section of the air-
craft gas turbine engine. Over the past thirty years,
nickel-base superalloys in particular have been found
to possess the optimum combination of properties for
this demanding application (1).

The widespread use of nickel-base alloys dates
back to the 1940's when they were first introduced as
heat-resistant materials in gas turbine engines (2).
These alloys had a nickel-chromium base and possessed a
combination of creep strength and oxidation resistance
which surpassed that of the then available stainless
steels. A major innovation occurred in superalloy de-
velopment during World War II (3) when titanium and
aluminum were added to the nickel-chromium solid solu-

1

tion strengthened superalloys to produce the precipita-
tion hardenable superalloys. These additions produced
the intermetallic compound known as γ', which is a
$Ni_3(Al,Ti)$ ordered FCC phase. It is from these
coherent precipitates that nickel-base superalloys
obtain their superior strengths.

Significant improvements in the high temperature
strength of superalloys were attained by compositional
adjustments and new processing techniques. During the
1950's, vacuum melting was introduced (4) because it
allowed the higher additions of aluminum and titanium
to raise the γ' volume fraction, and because it permit-
ted controlled additions of refractory elements for
solid solution strengthening. Through the mid-1960's,
continued alloy development further increased the γ'
volume fraction by reducing the chromium content.
However, the reduction in chromium content also de-
creased the oxidation resistance (5). Thus, it became
apparent that an alternative approach was needed to
attain higher usage temperatures for this family of
alloys.

Directional Solidification

A major breakthrough in the investment casting
process occurred with the introduction of unidirec-

tional solidification (6). This process provides a columnar grain structure in which the grain boundaries are oriented parallel to the major stress axis of the turbine blade. This columnar grain structure reduces the weakening influence of transverse grain boundaries and provides a creep resistance for directionally solidified (DS) superalloys which is superior to that for conventionally cast superalloys (6-9) with an equiaxed grain structure.

Columnar grain structures can be produced if heat is removed from the casting in one preferred direction during solidification. This preferential heat flow usually is achieved through the use of a water-cooled chill plate. This condition can be attained by pouring a superheated metal into the mold against the chill while concurrently establishing a suitable temperature gradient along the axial length of the mold with a furnace. Solidification starts at the chill in the form of an equiaxed structure, but the competitive growth between these randomly oriented equiaxed grains results in the development of a columnar structure with a preferred [001] orientation. It has been demonstrated (9-12) that the preferred [001] orientation of the columnar grains also contributes to the improvement in creep resistance of directionally solidified alloys.

The technology of unidirectional solidification has been developed to a high degree of sophistication. In the early Power-Down method (5,13-16), the solidification cycle was controlled by gradually reducing the power to the upper portion of an induction heater. A schematic diagram of this technique (13) is shown in Figure 1(a). Other techniques for heating the mold included electrical resistance heating (5) and the use of exothermic material (17).

High Rate Solidification, commonly known as the withdrawal process, was first introduced in 1971 (15), and is the predominant process used in the production of directionally solidified turbine airfoils (4,13, 14). In this process, the mold is mechanically withdrawn from the hot zone of the furnace, through a radiation baffle, and into a cooling chamber. Figure 1(b) is a schematic representation of this technique (13).

The Liquid Metal Cooling (LMC) technique has been developed more recently as another directional solidification process (18) and is illustrated in Figure 2 (13). In this process, the mold is lowered from the furnace hot zone, through a baffle, and into a cooling medium of rapidly circulating liquid tin. The LMC process makes it possible to grow dendritic structures

at substantially higher rates, thereby producing sig-
nificantly finer microstructures. Finally, the exo-
thermic DS process has been revived recently as a
viable casting alternative which simultaneously offers
significant reductions in turbine blade cost (19).

Single Crystal Production

The development of single crystal superalloys was
the next logical step after the production of direc-
tionally solidified columnar grained material. It had
been determined that the longitudinal grain boundaries
in columnar grained structures contributed to their
high temperature failure. Although these grain bound-
aries in general are parallel to the columnar growth
direction, they are not linear but instead follow
irregular paths between interlocking dendrite arms
(9,10). These grain boundaries contain small sections
transverse to the major stress axis which are suitable
locations for crack nucleation and growth. Thus, these
transverse sections are similar to the transverse grain
boundaries in conventionally cast material. Superalloy
single crystals do not contain deleterious grain bound-
aries, and thus permit still higher operating tempera-
tures to be attained in the aircraft gas turbine engine.

Single crystals can be grown in the same equipment

and with essentially the same solidificat:on techniques
as the directionally solidified superalloys. The major
difference is the placement of a multiple-turn con-
striction immediately above the initial growth zone, or
"starter" block of the casting. The starter is used to
establish columnar grain growth. As these grains grow
through the multiple-turn constriction, one [001] grain
survives the competitive growth process and continues
to grow into the blade section of the mold.

This competitive growth process favors the [001]
oriented grain because it is the direction of most
rapid growth for cubic metals (20-22). The fact that
the [001] orientation is naturally selected is fortu-
itous because this orientation provides the best combi-
nation of properties in the major stress axis of the
turbine blade (10,23). This favorable orientation, and
the lack of grain boundaries, are the major advantages
of single crystal turbine blades. At all temperatures,
[001] oriented single crystals exhibit both longer
stress rupture lives and lower minimum creep rates than
columnar grained material with a preferred [001] orien-
tation (10,23).

Mechanical Properties of Single Crystals

Tensile Properties

The influence of orientation on the tensile behavior of Mar-M200 and Mar-M247 single crystals has been studied previously (10,24). The compositions of these and other selected nickel-base superalloys are presented in Table I. The tensile behavior was rationalized on the basis of Schmid's Law which is illustrated in Figure 3 (25) and states that:

$$\tau = (P/A) \cos \phi \cos \lambda,$$

where τ is the critical resolved shear stress (CRSS); (P/A) is the measured yield strength; ϕ is the angle between the normal to the slip plane and the tensile axis; λ is the angle between the slip direction and the tensile axis; and $\cos \phi \cos \lambda$ is the Schmid factor. The slip system with the highest Schmid factor is generally the first operative slip system because it is the system most favorably oriented for slip. Thus, the magnitude of the Schmid factor is an indicator of the ease with which a material undergoes slip.

The operative slip system for tensile testing up to $760^\circ C$ has been found to be the $(111)[\bar{1}01]$ slip system (10,26,27). Deformation occurs by the shearing of the γ and γ' phases by $(a/2)<110>$ superlattice pairs (26). The

Schmid factor contours for this slip system are presented in Figure 4, where they have been superimposed on the standard [001] - [011] - [$\bar{1}$11] stereographic triangle. The solid lines in the figure delineate orientations of constant Schmid factor of the values indicated. The Schmid factor contours presented in this study all have been produced by the present investigator according to a simple graphical technique (28) described in the litera-ture.

The 0.02% yield strengths and percent elongations for the Mar-M247 single crystals tested between 23 and 760°C are presented as a function of initial orienta-tion in Figures 5(a) and (b), respectively (24). The data over this temperature range can be compared because the CRSS is virtually constant for the temperatures indi-cated, and thus the same slip system is operative. The Schmid factor contours from the [$\bar{1}$17] - [001] - [013] corner of the stereographic triangle in Figure 4 have been superimposed onto the tensile data in Figures 5(a) and (b). Comparison of these data with the Schmid factor contours demonstrates that single crystals with high Schmid factors are favorably oriented for slip and there-fore generally exhibit lower strengths and higher ductil-ities. Crystals with low Schmid factors generally ex-hibit higher strengths and lower ductilities. Thus, the

tensile behavior of single crystals is related to the Schmid factor in a straightforward manner.

Creep and Stress Rupture Properties

The stress rupture behavior is somewhat more complex tnan the tensile behavior of nickel-base superalloys and is not fully understood. Initial studies (10) on the orientation and temperature dependence of the stress rupture properties of Mar-M200 revealed that, at 750°C, a substantial improvement in the stress rupture life occurs for crystals with orientations near the [001] and [$\bar{1}$11]. Conversely, very short lives were exhibited by specimens oriented near the [011]. At 871°C, high stress rupture lives also were obtained near the [001] and [$\bar{1}$11] orientations, however the influence of orientation is less pronounced than it is at 760°C. At 982°C, crystallographic orientation was found to have even less infl ence on the stress rupture life. The reduction in the influence of orientation with increasing temperature is a result of additional slip systems becoming operative at more elevated temperatures (10,29). The underlying mechanisms whicn describe the influence of orientation on the stress rupture life have not been fully elucidated. The orientation dependence of the stress rupture behavior cannot be explained by the Schmid factors alone.

Similar anisotropic behavior of the stress rupture properties was exhibited for exothermically cast Mar-M247 single crystals (24). The stress rupture lives are presented as a function of orientation in Figures 6(a) and (b) for the Mar-M247 single crystals tested under two different conditions: $774^{\circ}C$ and 724 MPa; and $982^{\circ}C$ and 20. MPa. These figures also demonstrate along with the Mar-M200 data that the effect of initial orientation is much more pronounced at lower testing temperatures.

Mechanistic studies (26,30,31) were undertaken to examine creep deformation at 760 and $857^{\circ}C$ for Mar-M200 single crystals. At $760^{\circ}C$, primary creep was found to occur on the {111}<112> slip systems rather than on the {111}<110> slip systems. It was determined that (a/2)<112> dislocations are generated and then are dissociated into (a/6)<112> and (a/3)<112> partials. These (a/3)<112> partial dislocations then control primary creep by shearing the γ' precipitates by a diffusion-assisted process. Second-stage creep begins only after sufficient strain hardening occurs because of the interaction of {111}<112> slip systems. On the basis of activation energy studies (32), it was concluded that second-stage creep deformation occurs by slip on the {111}<110> slip systems and is controlled by the shearing of the γ' by (a/2)<110> dislocation pairs (31).

At 760°C (26), a short incubation period is re-
quired to generate the operative (a/2)<112> disloca-
tions. The incubation period is followed by a rapid
primary creep rate which is dependent on crystallographic
orientation. The orientation dependence of both the rate
and extent of primary creep was correlated with the
Schmid factors and the multiplicity of slip for the
{111}<112> systems. The primary creep strain and rate
increased as a function of orientation in the following
order: [001]; [001] - [011] boundary; region between the
[001] - [011] and [001] - [Ī11] boundaries; and [001] -
[Ī11] boundary. During primary creep, strain hardening
was large for multiple slip orientations and small for
single slip orientations.

For creep deformation at 857°C (31), it was found
that pairs of (a/2)<110> dislocations shear the γ' in
both primary and second-stage creep. The creep curves of
these crystals did not include an incubation period, and
the primary creep rate decreased continuously with time.
The differences in steady-state creep rates were more
striking as a function of orientation than were the pri-
mary creep strains. The orientation dependence of the
steady-state creep rate at 857°C was explained by the
nature of the dislocation junction reactions resulting
from {111}<110> slip for different orientations. It was

determined that crystals along the [001] - [Ī11] boundary had the lowest second-stage creep rates because of the formation of stable dislocation networks at the γ - γ' interfaces. The h'ghest steady-state creep rates were exhibited by crystals oriented along the [001] - [011] boundary as a consequence of the low probability for the formation of stable junction reactions for crystals of these orientations. However, the overall effect of anisotropy among these specimens tested at 857°C was less than the large orientation dependence of creep behavior at 760°C.

Tne c·eep rupture behavior at 982°C of the single crystal nickel-base superalloy designated as Alloy 444 (Table I) also has been examined (29). Unlike the Mar-M200 crystals at 857°C, little difference was founc among the specimens oriented near the [001] - [Ī11] and the [001] - [011] boundaries of the stereographic triangle. Analysis of the lattice rotations of the failed specimens showed rotations of less than 4˚. This indicates that slip is occurring on several slip systems at 982°C. No incubation period was observed, and the extent of primary creep was very limited. The empirical results indicated that single crystals of this alloy could be misoriented as much as 26˚ off the [001] with no loss in creep strength at 982°C.

Despite the advances made in identifying the mechanisms of creep deformation, the influence of orientation on stress rupture life is not fully understood. Furthermore, the stress rupture life data generated for nickel-base superalloy single crystals have been notably limited, particularly for orientations a few degrees off the [001] orientation. These orientations are currently being utilized in single crystal turbine blade applications. Typical criteria for acceptable single crystal turbine airfoils allow the orientations of the blade axes to range up to a designated maximum number of degrees from the [001] orientation. For example, a recently employed criterion specified 10° off the [001] as the maximum number of degrees off-axis allowed (33).

On the basis of the above discussion, it is clear that further investigation of the anisotropy of the stress rupture properties of nickel-base superalloy single crystals is warranted. The effects of anisotropy particularly for crystals with orientations near the [001] have important implications not only for the longitudinal properties, but for the transverse properties as well, because the root and lower portions of the turbine blade undergo significant stresses in directions transverse to the axis of the blade. It has been demonstrated (10,24) that the effect of crystallographic orientation

is much more pronounced at lower temperatures such as 760 and 774^{0}C. This latter temperature is representative of the temperature above the root in the lower portion of the turbine blade in current and advanced aircraft engines (34).

Thus far, mechanistic studies (26,31) have indicated differences in creep rupture behavior among orientations along the [001] - [$\bar{1}$11] and [001] - [011] boundaries of the stereographic triangle near the commercially desirable [001] orientation. Dislocation interactions have been cited as reasons for such differences between boundary orientations at 857^{0}C. However, the rotations that the crystals undergo during deformation which may actually lead to differences in dislocation interactions were not discussed. It is this more macroscopic cause which in particular requires additional consideration.

Statement of Purpose

The purpose of the present work was to attain an improved understanding of the orientation dependence of the stress rupture properties of Mar-M247 single crystals. This study evaluates the stress rupture properties generated for Mar-M247 single crystals and provides a unified analysis of these data as well as those reported for Mar-M200 (10,26). The improved fundamental understanding of the anisotropy provided by this study should assist in the successful implementation of single crystal airfoils.

MATERIAL AND EXPERIMENTAL PROCEDURE

Single Crystals

Eight single crystals* of Mar-M247 were grown by an adaptation of the exothermic process (33), and fifteen Mar-M247 single crystals** were produced by the withdrawal process. Chemical analyses were performed on several single crystals grown from both the exothermic and withdrawal processes. The compositions of the alloy are given in Table 1.

The 1.3 cm. diameter single crystal bars were solution treated in an argon atmosphere at $1232^{0}C$ for two hours and then argon quenched. Subsequently, the crystals were aged at $816^{0}C$ for 24 hours and air cooled to room temperature. Stress rupture specimens, with the configuration shown in Figure 7, were prepared by precision grinding.

----

* Produced by AiResearch Manufacturing Company of Arizona.
** Produced by TRW Metals - Turbine Components Division, Minerva, Ohio.

16

Mechanical Testing

Tensile tests were performed on single crystals produced by both the exothermic and withdrawal processes in order to fully characterize the material. These tests were performed at 23°C according to ASTM Specification E 8-69 (35). The crystals utilized had nearly identical orientations (within $\pm 1^{\circ}$) and exhibited similar tensile properties.

Stress rupture tests were performed on the exothermically cast single crystals, as well as on four of the crystals produced by the withdrawal process, in a constant load creep frame according to ASTM Specification E 139-70 (36). Figure 7 shows the three Pt/Pt-10 Rd thermocouples which were attached at the top, middle, and bottom of the specimen gage section to ensure that the temperature along the gage length was maintained at 774 $\pm$ 2°C. The stress level utilized for these tests was 724 MPa.

Constant load creep rupture tests were performed at 774 $\pm$ 2°C and 724 MPa on eleven of the crystals which were grown by the withdrawal process. Extensometer knife edges were placed in ridges at the extremes of the specimen gage section, as shown in Figure 7. Creep extensions were measured automatically with the extensometers and were recorded continuously with linear variable differen-

tial transformers (LVDT's) and strip chart recorders until specimen failure. All creep measurements obtained were calculated directly from the strip charts upon which extension versus time were plotted for each creep rupture test. The following data were obtained: instantaneous strain on loading, ϵ_0; incubation time, t_i; primary creep rate, $\dot{\epsilon}_p$; primary creep strain, ϵ_p; strain at onset of second-stage creep, ϵ_s; and minimum creep rate, $\dot{\epsilon}_m$.

Laue Back-Reflection X-ray Technique

The initial orientations of each of the machined specimens, as well as the final orientations of selected crystals after stress rupture testing, were determined by the Laue back-reflection X-ray technique. A failed specimen half of each single crystal was chosen. The grip end of each specimen half was used to obtain the initial orientation of the crystal, whereas the gage section yielded the final orientation of each crystal after mechanical testing.

The grip end was rough ground on SiC papers of 240, 320, 400, and 600-grit size and then mechanically polished with 0.3 and 0.05 μm alumina on cloth-covered wheels. The fracture surface of each specimen half was sliced off on a slow speed diamond saw, and the cross

section of the gage length behind the fracture surface was mounted in epoxy. Rough grinding of this cross section was performed on 600-grit SiC paper, and the intermediate and final mechanical polishings were accomplished in the same manner as that for the grip end.

The polished surfaces were etched in a solution of 30% concentrated HCl and 70% H_2O_2 (30 vol. %) after each step of the polishing sequence in order to remove any cold-worked material produced during polishing. This procedure permitted a sharp diffraction pattern to be obtained. The polished specimen halves were placed in a fixture designed to align the specimen axis parallel to the X-ray beam. Laue patterns were taken from the grip ends of all the specimens and from the gage sections of selected specimens. The initial orientations of all the single crystals and the final orientations of selected specimens were determined.

Microscopy

The structures of the Mar-M247 single crystals produced by both the exothermic method and withdrawal process were examined and characterized by light and scanning electron microscopy. The specimens used for metallographic examination were removed from sections closest to the chill of the 1.3 cm. diameter single crystal bars.

The single crystals had received a complete heat treatment. The specimens were mounted in bakelite and were ground and polished in the same manner as that described for the grip end in the previous section.

Light microscopy was performed on both longitudinal sections and cross sections of near cube-oriented single crystals. The samples were examined first in the unetched condition to check for microporosity. Next, the samples were etched with a solution containing 30% concentrated HCl and 70% H_2O_2 (30 vol. %) to reveal both the microstructure and the macrostructure, the latter of which was revealed with a somewhat longer etching time.

Scanning electron microscopy was performed on cross sections of the single crystals to examine the size, shape, and distribution of the γ' precipitate both in the dendrite centers and in the interdendritic regions. Two etchants were utilized in order to reveal the desired features. An etch consisting of 33 parts H_2O, 33 parts CH_3COOH, 33 parts HNO_3, and 1 part HF was applied by immersion. This solution preferentially etched the γ' precipitate. A staining etch containing 4.5 grams NH_4FHF, 1.1 grams $K_2S_2O_5$, 100 ml. H_2O, and 50 ml. HCl was applied over the first etch by immersing the specimen in the solution for one minute. This second etchant colored the dendrites, making them easily visible

under the scanning electron microscope.

The γ' size was determined by measuring the sides of these precipitates on the scanning electron micrographs taken at magnifications of 10,000X. The γ' precipitates located in the dendrite cores, as well as the coarse cuboidal γ' located in the interdendritic interstices, were examined and measured in this size determination.

RESULTS AND DISCUSSION

Structure of the Single Crystals

Examination of the fully heat treated specimens by
light and scanning electron microscopy revealed that the
single crystals produced by the exothermic method and the
withdrawal process were essentially the same in micro-
structure. Therefore in the discussion that follows, the
crystals resulting from the two different solidification
processes are not differentiated.

Although referred to as a "single crystal" mate-
rial, Mar-M247 contains several phases. Its structure
consists of ~60 volume percent of the coherent γ' precip-
itate in a matrix of γ, a nickel-rich solid solution.
The γ' phase has an ordered FCC structure based on
$Ni_3(Al,Ti)$ and is responsible for providing nickel-base
superalloys with much of their superior strength. The
interdendritic regions of Mar-M247 are interspersed
additionally with MC carbides and small amounts of the
$\gamma - \gamma'$ eutectic. Elemental segregation during solidi-
fication is responsible for the formation of the eutectic
constituent and MC carbides (11,37). Heat treatment of

this material partially removes segregation, refines the γ' dispersion in the γ matrix, and eliminates some of the γ - γ' eutectic. An example of the γ - γ' eutectic contained in the interdendritic region of a fully heat treated Mar-M247 single crystal is shown in the lower left corner of Figure 8. The eutectic is composed of massive γ' particles which are separated by thin lamellae of γ. The γ' is shown to be preferentially etched in all of the scanning electron micrographs presented.

Solute segregation not only promotes the formation of the γ - γ' eutectic and MC carbides but also affects the size of the γ' precipitate (37). Scanning electron microscopy shows clearly that the morphology of the γ' particles depends on the location within the dendritic structure. The micrograph in Figure 9(a) was taken at a magnification of 300X and shows the coring produced during solidification which remains after the material has been given a standard heat treatment. Figure 9(b) depicts the same area of the sample at 3000X and distinctly illustrates the change in γ' size at the interface between the dendrite core and interdendritic region.

The considerable differences in local solute composition (11) results in microstructural variations, because the solvus temperature is highest in the interdendritic regions where the solute content is higher

(14,38). Thus, precipitation of the γ' particles begins first and the γ' coarsens more in the interdendritic regions (39). Typical examples of the microstructure of a fully heat treated Mar-M247 single crystal in the dendrite core and in the interdendritic region are shown in Figures 10(a) and (b), respectively, at magnifications of 10,000X. The dendrite centers of all the single crystals examined have an average γ' particle size of about 0.28 µm, whereas the interdendritic regions contain large precipitates about 0.55 µm in size. The micrograph in Figure 10(b) shows that the interdendritic regions also contain fine γ' dispersed in between the relatively massive γ' after heat treatment. This fine γ' reprecipitates out when more aluminum and titanium are made available after the coarse γ' is partially redissolved during solution heat treatment (37).

In addition to the size difference, the shape of the γ' changes with respect to the location within the microstructure. The dendrite core shown in Figure 10(a) is composed of fairly regular cuboidal-shaped particles. However, Figure 10(b) shows that the large γ' precipitates in the interdendritic regions have a tendency to coalesce, appearing as groups of four in a polished surface. This ordered arrangement is actually a symmetrical cluster of eight cuboidal particles in three dimensions,

which has been described in detail as ogdoadically diced cubes that are cut by three mutually perpendicular planes (40). Figure 10(b) also shows that when the individual particles in the group become coarse, the extremities of the group become more irregular in shape.

Single crystals grown in the [001] orientation develop a unidirectional dendritic structure, because the [001] is the preferred direction of growth for dendrites in cubic metals. The typical macrostructure of a Mar-M247 single crystal grown in the cube direction is shown in Figures 11(a) and (b) for transverse and longitudinal sections, respectively. The primary dendrite arms are continuous in the [001] growth direction, as shown in the longitudinal section in Figure 11(b).

Mechanical Testing Data

Twenty-three Mar-M247 single crystals were stress rupture tested at 724 MPa and 774°C where the effect of anisotropy is prominent. The results are summarized in Table II. Eight of these single crystals had been grown by an exothermic process which provided crystals with orientations that were scattered throughout the standard stereographic triangle. Fifteen additional single crystals were grown by the withdrawal process. Creep extensions were recorded continuously during the stress rup-

ture testing of eleven of these fifteen additional crystals. This latter testing further established the stress rupture behavior for orientations near the commercially desirable [001].

The wide variations in the stress rupture lives of the Mar-M247 single crystals tested at 774°C and 724 MPa are shown in Figure 12 as a function of orientation. Extremely low lives are exhibited near the [011], extremely high lives occur near the [$\bar{1}$11], and high lives are associated with the [001] orientation. However, there is also a region just a few degrees off the [001] where appreciably shorter lives occur. It is these wide differences in stress rupture lives particularly near the [001] that need further consideration.

Schmid Factors

Comparison of the stress rupture data with the appropriate Schmid factor contours did not reveal a simple relationship. The mechanisms involved are somewhat more complex than those for tensile testing. The {111}<112> slip system is operative during first-stage creep in the intermediate temperature range of 760°C (24,26,31). The Schmid factor contours for the most highly stressed {111}<112> slip systems are illustrated in Figure 13. The X - Y line in Figure 13 is the divid-

ing line between the two {111}<112> slip systems which have the highest values of Schmid factor for orientations within the stereographic triangle. This X - Y line is approximately 25° from the [001]. The ($\bar{1}$11)[1$\bar{1}$2] slip system is operative for orientations within the triangle borders which lie to the left of the X - Y line; the (111)[$\bar{2}$11] slip system is operative for orientations within the triangle borders which lie to the right of the X - Y line.

The crystal with the approximate [$\bar{1}$11] orientation in Figure 12 exhibited the highest stress rupture life in part because the [$\bar{1}$11] provides the lowest Schmid factor of 0.31 for first-stage creep. As shown in Figure 12, crystals with approximate [001] orientations had lives greater than 100 hours, whereas crystals with orientations near the [011] had lives of one hour or less. In this case, the Schmid factors do not explain the large differences in the stress rupture lives, because the [001] and [011] have equivalent Schmid factors of 0.47 for first-stage creep. Furthermore, the lives are appreciably shorter for crystals oriented a few degrees off the [001] compared with those of approximate [001] orientations, as shown in Figure 12. The [001] and the region of the triangle near the [001] have similar Schmid factors. Therefore, the Schmid factors cannot be utilized

to explain the differences in the stress rupture lives of these single crystals.

Lattice Rotations

During plastic deformation, single crystals rotate toward their slip direction, as is shown schematically for the gage section of the bar in Figure 14 (41). The directions of rotation within the stereographic triangle for the {111}<112> and (111)[$\bar{1}$01] slip systems are shown in Figures 15(a) and (b), respectively. For the {111}<112> slip system, the [001] - Y and X - [$\bar{1}$11] boundaries both represent regions of duplex slip in the standard stereographic triangle. Duplex slip regions are positions of crystallographic symmetry in which the Schmid factors are equivalent for two slip systems. This allows equal slip activity on two slip systems.

In the 760°C temperature regime, single crystals oriented within the borders of the stereographic triangle initially deform during stress rupture testing by easy glide and rotate, as indicated by the arrows in Figure 15(a), under single slip until one of the duplex slip boundaries is reached, or nearly reached. The transition from first-stage to second-stage creep occurs only after sufficient intersecting slip between the {111}<112> slip systems strain hardens the material (26,42). During

second-stage creep, the (111)[Ī01] slip system becomes
operative (31), and the crystals rotate in the directions
shown in Figure 15(b).

The lattice rotations determined by X-ray analysis
for selected specimens stress rupture tested at 774°C
and 724 MPa are illustrated in Figure 16. The solid dots
indicate the initial orientations of the crystals prior
to testing, and the x's represent the orientations at the
culmination of the test. The numbers associated with the
rotations represent the stress rupture lives of the crys-
tals in hours. Figure 16 shows two portions of the
stereographic triangle which have been drawn on two dif-
ferent scales. The [001] corner in Figure 16(a) has been
enlarged to show the detail of the rotations up to 10°
from the [001] orientation.

The {111}<112> slip system appears to be operative
for the single crystals when the lattice rotations in
Figure 16 are compared to the rotations depicted in Fig-
ure 15(a). As illustrated in Figure 16(b), Specimens 2
and 158 were oriented initially near the [011] orienta-
tion and had lives of 0.5 hours and one hour, respec-
tively. These crystals rotated through regions of high
Schmid factor toward their slip direction during first-
stage creep and failed before reaching the X - [Ī11]
boundary. The creep curve of Specimen 2 is illustrated

in Figure 17 and shows that the crystal actually failed
during first-stage creep. Thus, no transition to
steady-state creep occurred prior to failure. Specimen
147 is shown in Figure 16(b) as having life of 138
hours. Within experimental error, this crystal rotated
to the X - [Ī11] boundary prior to failure. In contrast,
Crystal 157 in Figure 16(b) had an approximate [Ī11] ori-
entation and exhibited the longest stress rupture life of
1242 hours. This behavior is attributed to the multiple
slip and to the minimum in Schmid factor that occur for a
crystal having this orientation.

The rotations of the single crystals having orien-
tations near the [001] are illustrated in Figure 16(a).
Specimens 1 and B were oriented closest to the [001] and
had stress rupture lives of 179 and 141 hours, respec-
tively. Although both crystals were oriented initially
for intersecting slip along the [001] - Y boundary, they
were not located in a low Schmid factor region. There-
fore, the two lives which resulted were significantly
lower than that of the [Ī11] crystal in Figure 16(b).
The creep curve of Specimen B is illustrated in Figure 17
and shows regions of primary, steady-state, and tertiary
creep. In contrast, Specimens ES and J were oriented
approximately 10° off the [001] in the single slip region
between the borders of the stereographic triangle in

Figure 16(a). These crystals were able to rotate to the [001] - Y boundary prior to the end of the creep rupture tests and exhibited lives of 53 and 26 hours, respectively. The creep curve of Specimen J in Figure 17 shows that the transition to steady-state creep was obtained prior to failure, although the slope of the second-stage creep regime was very high compared to that of Specimen B which had an approximate [001] orientation.

The creep rupture behavior of crystals oriented along the [001] - X boundary is similar to the behavior of crystals oriented within the borders of the stereographic triangle. Crystals initially oriented along this single slip [001] - X boundary deform by extensive easy glide and rotate toward the multiple slip [001] orientation. As illustrated in Figure 16(a), X-ray analysis showed that Specimen C rotated along the [001] - X boundary from 8° to 1° off tne [001] during mechanical testing. This final orientation is further substantiated by the glide calculations presented in Appendix A, where it was also shown that this crystal could not have reached the multiple slip [001] orientation. As a result, the creep curve of Specimen C shows that a linear slope, characteristic of the steady-state creep regime, was not obtained. Thus, it appears that the transition into steady-state creep did not occur, and the specimen

exhibited a very short life of 14 hours. However, Specimens D, 33, and HS were oriented initially within 5.5° from the [001] along the [001] - X boundary. These crystals were able to rotate into intersecting slip regions of the stereographic triangle and had lives ranging from 59 to 80 hours. The creep curves of these crystals, in contrast to Crystal C, exhibited regions of primary, steady-state, and tertiary creep, as illustrated by the creep curve of Specimen HS in Figure 17.

Creep Rupture Data

To provide further insight into the influence of orientation, the creep rupture data which were generated for eleven of the twenty-three single crystals tested are discussed in some detail below. These data are summarized in Table III, and the following properties are included: instantaneous strain on loading, ϵ_0; incubation time, t_i; primary creep strain, ϵ_p; primary creep rate, $\dot{\epsilon}_p$; strain at the onset of second-stage creep, ϵ_s; and minimum creep rate, $\dot{\epsilon}_m$. The methods for measuring these creep data are described in Appendix B.

The primary creep strain, primary creep rate, strain at the onset of second-stage creep, and minimum creep rate are plotted as a function of orientation in

Figures 18(a)-(d) for the Mar-M247 single crystals creep rupture tested at 774°C and 724 MPa. The creep rates and strains of the crystals within 10.5° of the [001] increased with orientation in the following order: [001]; orientations along the [001] - [011] boundary; orientations between the [001] - [011] and [001] - [$\bar{1}$11] boundaries; and orientations along the [001] - [$\bar{1}$i1] boundary. The [001] crystal was initially oriented for multiple slip, and the lowest values of ϵ_p and $\dot{\epsilon}_p$ were observed at this orientation. The [001] - [011] boundary represents duplex slip orientations, and intersecting slip occurs for crystals oriented along this boundary. Low values of ϵ_p, $\dot{\epsilon}_p$, ϵ_s, and $\dot{\epsilon}_m$ occurred for these orientations, and high lives resulted. In contrast, crystals oriented between the [001] - [$\bar{1}$11] and [001] - [011] boundaries and crystals oriented along the [001] - [$\bar{1}$11] boundary exhibited the highest creep strains and rates and the lowest creep rupture lives. These crystals deform by single slip until the duplex slip [001] - [011] boundary is reached.

An example of the importance of developing intersecting slip is demonstrated by comparing the creep data of Specimens C and ES in Table III and their corresponding rotations in Figure 16(a). Both crystals represent single slip orientations. However, Specimen C was ori-

ented 8° off the [001] along the [001] - [Ī11] boundary, and Specimen ES was 10.5° off the [001] between the borders of the stereographic triangle. Although oriented farther away from the [001], Specimen ES actually was oriented closer to the [001] - [011] boundary. Crystal ES had lower creep rates and strains than Crystal C and exhibited a stress rupture life which was four times longer than that of Crystal C.

Mar-M200 Data

The anisotropic behavior of the Mar-M200 single crystals creep rupture tested at $760°C$ and 689 MPa (26) is in agreement with tnat of the Mar-M247 data generated in this study. The Mar-M200 data are presented as a function of orientation in Figures 19(a)-(c). In particular, Figure 19(a) shows rather strikingly for crystals 16 to 18° off the [001] that the primary creep strain substantially decreased from 12.5% along the single slip [001] - [Ī11] boundary, to 6.3% between the triangle borders, and finally to 2.2% along the duplex slip [001] - [011] boundary.

Further substantiation of the stress rupture behavior was provided by the Mar-M200 single crystals tested at $760°C$ and 689 MPa (10). Tne stress rupture lives are shown as a function of orientation in Figure 20

(10). There were two crystals of particular interest, both of which were oriented approximately 12° off the [001]. The crystal which was oriented closer to the duplex slip [001] - [011] boundary had a life of 466 hours, whereas the crystal which was oriented closer to the single slip [001] - [$\bar{1}$11] boundary had a life of only 12 hours. Thus, an order of magnitude difference exists between the lives of two crystals, both oriented the same number of degrees from the [001], but oriented in different directions from the [001]. Furthermore, it appears from these experimental data plotted in Figure 20 that crystals may be oriented farther off-axis along the [001] - [011] boundary than crystals with equivalent stress rupture lives along the [001] - [$\bar{1}$11] boundary.

Although the actual lattice rotations were not determined in the Mar-M200 study (10), single slip was confirmed by the present investigator for the 12-hour life specimen by computing the elongation necessary to reach the duplex slip [001] - [011] boundary. The details of this computation are presented in Appendix A. The measured elongation after failure listed for this 12-hour life specimen was 10.3% (10); however, the elongation necessary to obtain duplex slip regions of the triangle was computed in Appendix A to be 25.4%. Clearly, this specimen never reached the duplex slip [001] -

[011] ooundary, and an extremely short stress rupture
life resulted for this crystal.

Factors Influencing Rupture Lives

Based on the stress rupture lives, creep rupture
data, and lattice rotations for Mar-M247 and the empiri-
cal data reported for Mar-M200 (10,26), it was deter-
mined that the primary factor which influenced the stress
rupture lives of the single crystals was the amount of
lattice rotation required to produce intersecting slip.
The lattice rotations influence the lives by directly
affecting the amount of strain that the crystal undergoes
during primary creep. During first-stage creep, the
single crystal deforms by easy glide, and the material
can elongate appreciably for single slip orientations, as
exemplified by Specimen C in Figure 17. The transition
from first-stage to second-stage creep begins only after
intersecting slip sufficiently strain hardens the mate-
rial. Therefore, second-stage creep cannot hegin until
the crystal has rotated to, or nearly to, the [001] - Y
or the X - [$\bar{1}$11] duplex slip boundary.

On the basis of the analysis described above, it
was hypothesized that the smaller the rotation required
to initiate intersecting slip, the sooner second-stage
creep will begin, and the longer the stress rupture life

will be. Smaller amounts of first-stage creep provide a
smaller reduction in the load-bearing cross section of
the specimen prior to the onset of steady-state creep.
Thus, the effective stress level at the beginning of
steady-state creep should be lower, and the stress rup-
ture life should be longer, for smaller amounts of pri-
mary creep.

The effective stress level at the onset of second-
stage creep for the Mar-M247 single crystals creep rup-
ture tested at $774^{\circ}C$ and a nominal stress of 724 MPa
was found to be influenced greatly by crystallographic
orientation. The details of this computation are given
in Appendix C. The effective stress level at the onset
of steady-state creep ranged from 753 MPa for Specimen B,
which had an approximate [001] orientation, to 790 MPa
for Specimen C, which was oriented 8° off the [001] along
the single slip [001] - X boundary. Specimen B had an
$\dot{\epsilon}_m$ equal to 2.03 $\times$ 10^{-4} hr.$^{-1}$ and a 141 hour life;
Specimen C had an $\dot{\epsilon}_m$ equal to 15.2 x 10^{-4} hr.$^{-1}$ and
a 14 hour life. Thus, a higher effective stress level at
the onset of second-stage creep corresponded to a higher
steady-state creep rate. Since the rupture lives of most
metals are inversely proportional to the steady-state
creep rates (31), any increase in this creep rate will
shorten the life of the crystal. Thus, the rupture lives

will be longer for smaller amounts of rotations to intersecting slip regions, because the effective stress levels will be lower for smaller amounts of primary creep.

In view of the above, the empirical observations of the stress rupture behavior of the Mar-M247 single crystals can be explained by the lattice rotations which the crystals underwent during mechanical testing at 774°C. Specimens oriented along directions of high symmetry, such as the approximate [$\bar{1}$11] and [001] orientations of Specimens 157 and B, respectively, exhibited the longest stress rupture lives because they were initially oriented for intersecting slip. Crystals which required large rotations to become oriented for intersecting slip, such as Specimens C, 2, and 158, had the shortest lives because they did not benefit from the strengthening effects of intersecting slip and second-stage creep was not obtained. Crystals oriented such that small elongations caused them to rotate into intersecting slip orientations exhibited intermediate lives.

Potential Commercial Applications

Based on a consideration of the lattice rotations, the creep and stress rupture data, and the Schmid factors for the Mar-M247 single crystals stress rupture tested at 774°C, the standard [001] - [011] - [$\bar{1}$11] stereographic

triangle was divided into several regions which were rank ordered according to stress rupture life for this temperature regime. This plot shown in Figure 21 indicates that the longest lives were exhibited by crystals having orientations near the $[\bar{1}11]$; long lives were exhibited by crystals having orientations near the [001]; and the shortest lives were exhibited by crystals near the [011]. The single crystal data generated in the present study agree reasonably well with the plot. Comparison of the creep rupture data for the Mar-M200 single crystals (10,26) shown in Figures 19-20 with this plot provides further verification of its validity.

Those crystals having orientations within about 25° of the [001] exhibited significantly longer lives when their orientations were closer to the [001] - [011] boundary of the stereographic triangle than to the [001] - $[\bar{1}11]$ boundary. It was determined that crystals oriented closer to the [001] - [011] boundary do not have to rotate as far before reaching intersecting slip regions during first-stage creep. Accordingly, the plot in Figure 21 predicts low lives in the region of the triangle greater than 7° off the [001] in the [001] - $[\bar{1}11]$ direction. This latter finding in particular has commercial significance. Although the $[\bar{1}11]$ orientation may be the most creep-resistant in this temperature regime,

crystals with orientations near the [001] are utilized for most single crystal turbine applications, because the [001] provides high stress rupture lives and excellent thermal fatigue resistance as a result of its low elastic modulus (10).

Typical criteria for acceptable single crystal turbine airfoils allow the orientations of the blade axes to range up to a designated maximum number of degrees from the [001] orientation. For example, a recently employed criterion specified 10° off the [001] as the maximum number of degrees off-axis allowed (33). According to Figure 21, this particular pass-fail standard encompasses regimes of the stereographic triangle which provide both very good and poor stress rupture lives. Furthermore, a criterion of this type would accept a crystal which exhibited a 12-hour life under the testing conditions utilized for the Mar-M200 crystals in Figure 20 (10) and would reject another crystal, tested under the same conditions, with an orientation which provided a 725-hour life.

It was determined in this study that the direction off the [001], as well as the number of degrees off the [001], has a major influence on the stress rupture lives of single crystals in this temperature regime. Therefore, it may be appropriate to incorporate the effect of

the direction off the [001] when establishing pass-fail
criteria for acceptable single crystal turbine blades.
Thus, the plot of suggested regimes of stress rupture
lives for Mar-M247 and Mar-M200 single crystals in Figure
21 should assist in establishing standards for commer-
cially acceptable orientations of single crystal turbine
airfoils.

CONCLUSIONS

1. For stress rupture testing at 774°C, crystals which required large rotations to become oriented for intersecting slip had the shortest lives; those which required little or no rotations had the longest lives.

2. The amount of lattice rotation required for a crystal to become oriented for intersecting slip directly influences the amount of strain that the crystal undergoes during primary creep, because steady-state creep does not begin until after the onset of intersecting slip. The smaller the primary creep strain is, the smaller the reduction in load-bearing cross section will be, and the lower the effective stress level will be at the onset of steady-state creep.

3. Although crystals near the [001] and [$\bar{1}$11] were both favorably oriented for intersecting slip at 774°C, the [$\bar{1}$11] orientation provided much longer stress rupture lives because of lower Schmid factors.

4. Crystals having orientations within about 25° of the [001] exhibited longer lives when oriented closer

to the [001] - [011] boundary of the stereographic tri-
angle than to the [001] - [$\bar{1}$11] boundary during stress
rupture testing at 760 and 774°C.

5. It may be appropriate to incorporate the effect
of direction off the [001], as well as the number f de-
grees off the [001], when establishing pass-fail criteria
for acceptable single crystal turbine blades.

REFERENCES

(1) D. N. Duhl and E. R. Thompson: "Directional Struc-
     tures for Advanced Aircraft Turbine Blades,"
     J. Aircraft, June 1977, vol. 14, pp. 521-526.

(2) W. F. Simmons: "Current and Future Materials Usage
     in Aircraft Gas Turbine Engines," MCIC 73-14,
     p. 1, Battelle Memorial Institute, June 1973.

(3) W. A. Owczarski: "Process and Metallurgical Fac-
     tors in Joining Superalloys and Other High
     Service Temperature Materials," in Advanced
     Manufacturing Techniques in Joining of Aero-
     space Materials, p. 3-3, AGARD, Sept. 1977.

(4) F. L. VerSnyder and E. R. Thompson: "Superalloys
     for Gas Turbines – Another 20 Years ," Climax
     Molybdenum Co. Conference for Alloys For the
     80's, Ann Arbor, Mich., June 17-18, 1980, in
     press.

(5) F. L. VerSnyder and M. F. Shank: "The Development
     of Columnar Grain and Single Crystal High Tem-
     perature Materials Through Directional Solidi-
     fication," Mater. Sci. Eng., 1970, vol. 6,
     pp. 213-247.

(6) F. L. VerSnyder and R. W. Guard: "Directional
     Grain Structures for High Temperature
     Strength," Trans. ASM, 1960, vol. 52,
     pp. 485-493.

(7) B. J. Piearcey and F. L. VerSnyder: "New Casting
     Technique Strengthens Turbine Components,"
     SAE J., June 1966, vol. 74, no. 6, pp. 84-87.

(8) F. L. VerSnyder, R. B. Barrow, L. W. Sink, and
     B. J. Piearcey: "Directional Solidification in
     the Precision Casting of Gas-Turbine Parts,"
     Modern Cast., Sept. 1967, vol. 52, no. 6,
     pp. 68-75.

(9) B. J. Piearcey and B. E. Terkelsen: "The Effect of Unidirectional Solidification on the Properties of Cast Nickel-Base Superalloys," Trans. TMS-AIME, Aug. 1967, vol. 239, pp. 1143-1150.

(10) B. H. Kear and B. J. Piearcey: "Tensile and Creep Properties of Single Crystals of the Nickel-Base Superalloy Mar-M200," Trans. TMS-AIME, Aug. 1967, vol. 239, pp. 1209-1215.

(11) B. J. Piearcey, B. H. Kear, and R. W. Smashey: "Correlation of Structure with Properties in a Directionally Solidified Nickel-Base Super-alloy," Trans. ASM, 1967, vol. 60, pp. 634-645.

(12) B. H. Kear and A. F. Giamei: "Manipulation of Superalloy Microstructures and Properties By Advanced Processing Techniques," in Fundamental Aspects of Structural Alloy Design, R. I. Jaffe and B. A. Wilcox, eds., pp. 461-485, Plenum Publishing Corporation, New York, 1977.

(13) C. P. Sullivan, A. F. Giamei, and F. L. VerSnyder: "Some Aspects of Directional Solidification in the Production of Superalloy Ingots," Fifth Int'l. Symp. on Electroslag and Other Special Melting Technologies - Part III, G. H. Bhat and A. Simkovich, eds., pp. 525-594, Carnegie-Mellon Institute of Research, Pittsburgh, 1975.

(14) A. F. Giamei, E. H. Kraft, and F. D. Lemkey: "The Art and Science of Unidirectional Solidification," in New Trends in Materials Processing, C. S. Hartley, ed., pp. 48-97, American Soc. for Metals, Metals Park, Ohio, 1976.

(15) A. F. Giamei and J. S. Erickson: "Computer Applications in Directional Solidification Processing," Third Int'l. Symp. on Superalloys, Seven Springs, PA, Sept. 1976, B. H. Kear, et. al., eds., pp. 405-424, Claitor's Publishing Division, Baton Rouge, 1976.

(16) J. E. Northwood: "Improving Turbine Blade Performance by Solidification Control," Metallurgia, July 1979, pp. 437-442.

(17) M. C. Flemings, R. V. Barone, S. Z. Uram, and
      H. F. Taylor: "Solidification of Steel Cast-
      ings and Ingots," Trans. Am. Foundrymen's Soc.,
      1961, vol. 69, pp. 422-435.

(18) A. F. Giamei and J. G. Tschinkel: "Liquid Metal
      Cooling: A New Solidification Technique,"
      Met. Trans., Sept. 1976, vol. 7, pp. 1427-1434.

(19) G. S. Hoppin, III, M. Fujii, and L. W. Sink: "De-
      velopment of Low-Cost Directionally Solidified
      Turbine Blades," Fourth Int'l. Symp. on Super-
      alloys, Seven Springs, PA, Sept. 1980, J. K.
      Tien, et. al., eds., pp. 225-234, American
      Society for Metals, Metals Park, Ohio, 1980.

(20) B. Chalmers: in Principles of Solidification,
      p. 117, John Wiley & Sons, Inc., New York,
      1964.

(21) M. C. Flemings: in Solidification Processing,
      p. 73, McGraw-Hill Book Company, New York,
      1974.

(22) G. A. Chadwick: "A Hard-Sphere Model of Crystal
      Growth," Metal Sci. J., Sept. 1967, vol. 1,
      pp. 132-139.

(23) F. L. VerSnyder and B. J. Piearcey: "Single Crys-
      tal Alloy Extends Turbine Blade Service Four
      Times," SAE J., Aug. 1966, vol. 74, no. 8,
      pp. 36-42.

(24) R. A. MacKay, R. L. Dreshfield, and R. D. Maier:
      "Anisotropy of Nickel-Base Superalloy Single
      Crystals," Fourth Int'l. Symp. on Superalloys,
      Seven Springs, PA, Sept. 1980, J. K. Tien,
      et. al., eds., pp. 385-394, American Society
      for Metals, Metals Park, Ohio, 1980.

(25) G. E. Dieter: in Mechanical Metallurgy, 2nd ed.,
      p. 128, McGraw-Hill Book Company, New York,
      1976.

(26) G. R. Leverant and B. H. Kear: "The Mechanism of
      Creep in Gamma Prime Precipitation-Hardened
      Nickel-Base Alloys at Intermediate Tempera-
      tures," Met. Trans., Feb. 1970, vol. 1,
      pp. 491-498.

(27) S. M. Copley and B. H. Kear: "Temperature and Orientation Dependence of the Flow Stress in Off-Stoichiometric Ni_3Al (γ' Phase)," Trans. TMS-AIME, July 1967, vol. 239, pp. 977-984.

(28) C. S. Hartley and J. P. Hirth: "Resolution of Stresses in Single-Crystal Deformation," Trans. TMS-AIME, July 1965, vol. 233, pp. 1415-1419.

(29) D. N. Duhl, M. Gell, A. F. Giamei, and G. R. Leverant: "Deformation and Fracture of Advanced Anisotropic Superalloys," AFOSR Contract No. F44620-76-C-0028, Interim Technical Report, Nov. 1977.

(30) B. H. Kear, G. R. Leverant, and J. M. Oblak: "An Analysis of Creep-Induced Intrinsic/Extrinsic Fault Pairs in a Precipitation Hardened Nickel-Base Alloy," Trans. Quart. ASM, 1969, vol. 62, pp. 639-650.

(31) G. R. Leverant, B. H. Kear, and J. M. Oblak: "Creep of Precipitation-Hardened Nickel-Base Alloy Single Crystals at High Temperatures," Met. Trans., Jan. 1973, vol. 4, pp. 355-362.

(32) J. K. Tien, B. H. Kear, and G. R. Leverant: "On the High Activation Energy for Steady State Creep of Particle Strengthened Systems," Scripta Met., Feb. 1972, vol. 6, pp. 135-139.

(33) T. E. Strangman, G. S. Hoppin III, C. M. Phipps, K. Harris, and R. E. Schwer: "Development of Exothermically Cast Single-Crystal Mar-M247 and Derivative Alloys," Fourth Int'l. Symp. on Superalloys, Seven Springs, PA, Sept. 1980, J. K. Tien, et. al., eds., pp. 215-224, American Society for Metals, Metals Park, Ohio, 1980.

(34) D. N. Duhl: Personal Communication, Sept. 1980.

(35) E 8-69: "Standard Methods of Tension Testing of Metallic Materials," in 1974 Annual Book of ASTM Standards, Part 10, pp. 90-110, American Society for Testing and Materials, Philadelphia, 1974.

(36) E 139-70: "Standard Recommended Practice for Conducting Creep, Creep-Rupture, and Stress-Rupture Tests of Metallic Materials," in 1974 Annual Book of ASTM Standards, Part 10, pp. 229-245, American Society for Testing and Materials, Philadelphia, 1974.

(37) J. J. Jackson, M. J. Donachie, R. J. Henricks, and M. Gell: "The Effect of Volume Percent of Fine γ' on Creep in DS Mar-M200 + Hf," Met. Trans., Oct. 1977, vol. 8, pp. 1615-1620.

(38) T. Z. Kattamis and J. C. Lecomte: "A Novel Method for the Establishment of Solvus Surfaces as Demonstrated with Nickel-Base Alloys," J. Mater. Sci., Dec. 1978, vol. 13, pp. 2731-2736.

(39) G. D. Merz, T. Z. Kattamis, and A. F. Giamei: "Microsegregation and Homogenization of Ni - 7.5 wt% Al - 2.0 wt% Ta Dendritic Monocrystals," J. Mater. Sci., Mar. 1979, vol. 14, pp. 663-670.

(40) J. H. Westbrook: "Precipitation of Ni_3Al from Nickel Solid Solution as Ogdoadically Diced Cubes," Zeits fur Krist, 1958, vol. 110, p. 1.

(41) R. H. Hertzberg: in Deformation and Fracture Mechanics of Engineering Materials, p. 85, John Wiley & Sons, New York, 1976.

(42) G. R. Leverant and D. N. Duhl: "The Effect of Stress and Temperature on the Extent of Primary Creep in Directionally Solidified Nickel-Base Superalloys," Met. Trans., March 1971, vol. 2, pp. 907-908.

(43) E. Schmid and W. Boas: in Plasticity of Crystals, pp. 57-58, F. A. Hughes & Co. Limited, London, 1950.

(44) D. K. Bowen and J. W. Christian: "The Calculation of Shear Stress and Shear Strain for Double Glide in Tension and Compression," Philos. Mag., Aug. 1965, vol. 12, 8th series, no. 116, pp. 369-378.

TABLES

50

TABLE 1
COMPOSITIONS OF SELECTED NICKEL-BASE SUPERALLOYS (wt. %)

ELEMENTS	Mar-M200[a]	Mar-M200[b]	Alloy 444[c]	Mar-M247[d]	Mar-M247[e]
C	0.15	~50ppm	-	0.13	0.14
Cr	9.0	8.95	8.6	8.3	7.9
Co	10.0	10.55	-	9.9	9.5
Ti	2.0	1.65	1.98	0.93	0.96
Al	5.0	4.65	5.1	5.6	5.8
W	12.5	11.85	11.1	10.2	9.6
Zr	0.05	0.041	-	0.06	0.03
B	0.015	0.011	-	0.018	0.013
Fe	1.5 max	-	-	0.10 max	0.10 max
Nc	-	0.61	0.91	0.05 max	0.05 max
Mc	-	-	-	0.72	0.76
Ta	-	-	-	2.96	3.06
Hf	-	-	-	1.23	1.50
Ni	bal.	bal.	bal.	bal.	bal.

a   Utilized in Ref. 10.

b   Utilized in Refs. 26, 30, 31. Weight percent
    listed is an average of the compositional range.

c   Utilized in Ref. 29.

d   Utilized in Ref. 24 and in the present study
    (exothermic process).

e   Utilized in the present study (withdrawal
    process).

TABLE II

STRESS RUPTURE DATA OF MAR-M247 SINGLE CRYSTALS

TESTED AT 774°C and 724 MPa

SPECIMEN	LIFE, hr	ELONG., percent	R.A., percent	ORIENTATION, DEGREES FROM: [001]	[011]
1	179	16	15	3	42
72	26	9	12	7	38.5
74	21	11	13	10	36
123	37	12	15	8	37.5
128	20	8	12	28	17
147	138	8	15	45	28
157	1242	11	12	52.5	34.5
158	1	24	28	39	7
2	0.5	35	31	43	6.5
C	14	11	11	8	39.5
J	26	13	13	9.5	36
X	41	12	10	5.5	40.5
ES	53	13	13	10.5	35
F	53	13	12	5.5	41
D	59	10	9	2	43.5
33	74	12	10	4	42
HS	80	12	10	5.5	41
7S	82	12	11	7.5	39
6	90	11	14	4	41.5
G	98	12	10	5	40
A	109	12	10	1.5	43.5
B	141	14	13	2	43

TABLE III
CREEP RUPTURE DATA OF MAR-M247 SINGLE CRYSTALS
TESTED AT 774°C and 724 MPa

SPECIMEN	ε_0 $\times10^{-3}$	t_i, min	$\dot{\varepsilon}_p$, $\times10^{-1}$ hr^{-1}	ε_p, percent	ε_s, percent	$\dot{\varepsilon}_m$, $\times10^{-4}$ hr^{-1}	LIFE, hr	ORIENTATION, DEGREES FROM: [001]	[001]
2	5.4	14	8.50	34.7	-	-	0.5	43	6.5
C	9.1	13	1.68	5.91	9.20	15.18	14	8	39.5
J	2.4	19	1.64	5.48	6.95	11.49	26	9.5	36
ES	7.8	25	1.60	5.37	8.67	7.74	53	10.5	35
F	8.9	74	1.70	4.61	7.08	5.79	53	5.5	41
D	8.1	13	1.34	2.59	5.19	6.29	59	2	43.5
33	9.6	17	1.02	2.61	5.81	5.19	74	4	42
MS	4.9	24	0.87	3.71	6.55	4.95	80	5.5	41
O	6.7	26	0.24	2.04	4.19	3.02	-*	0	45
G	7.3	23	0.95	2.67	3.97	3.61	98	5	40
B	7.6	28	0.73	2.20	4.97	2.03	141	2	43

*furnace malfunctioned.

ε_0 = instantaneous strain on loading.

t_i = incubation time.

$\dot{\varepsilon}_p$, ε_p = primary creep rate and strain, respectively.

ε_s = strain at onset of steady-state creep.

$\dot{\varepsilon}_m$ = minimum creep rate.

FIGURES
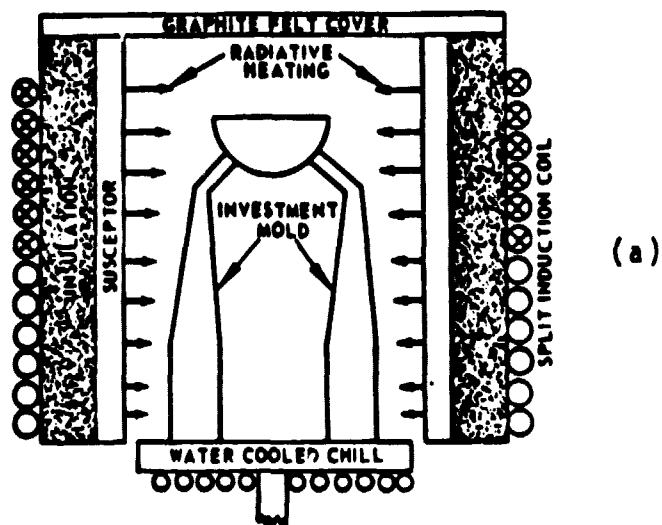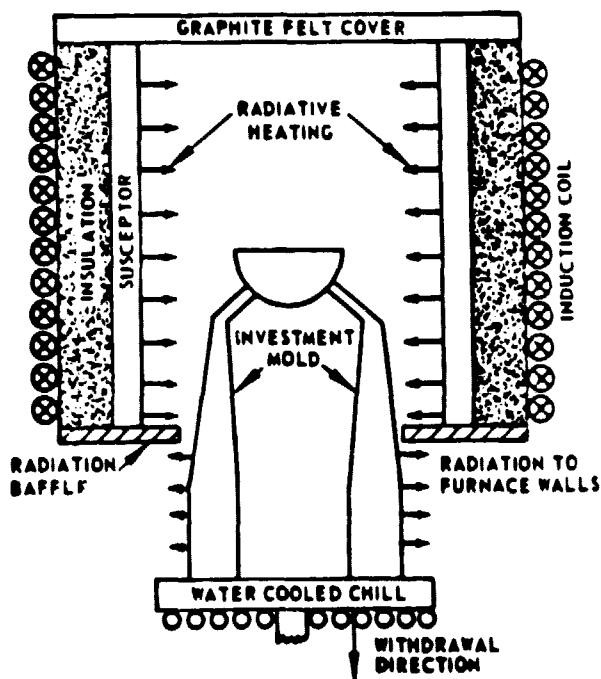
Figure 1. Schematic representation of the techniques used in the unidirectional solidification of superalloys: (a) Power Down process; and (b) High Rate Solidification, or withdrawal, process (13). X indicates power on to induction coil.
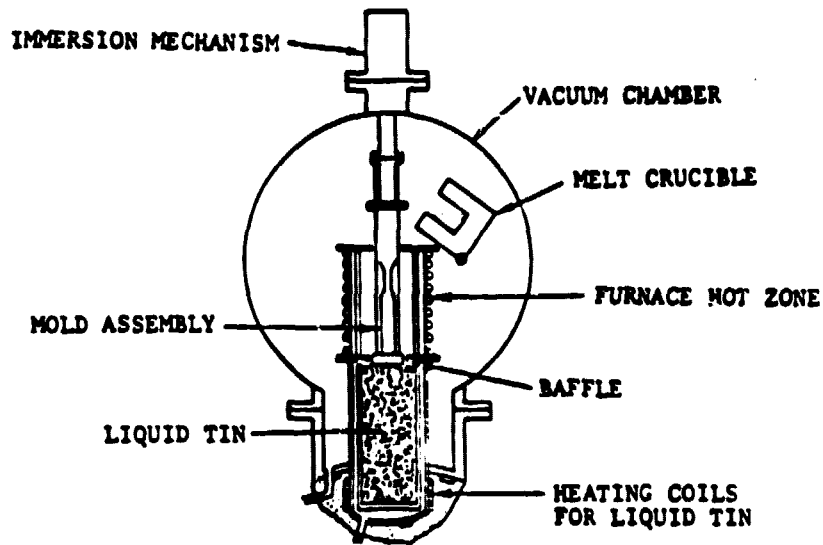
Figure 2. Schematic representation of the apparatus
used to make castings by the Liquid Metal
Cooling process (13).
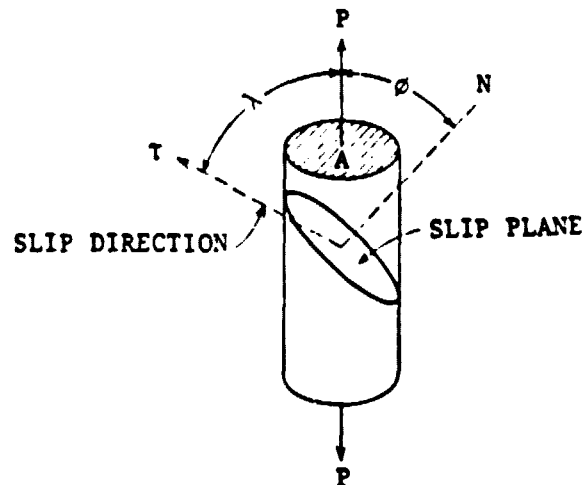
Figure 3. Schematic diagram for description of the
angles, λ and ϕ, used in Schmid's Law for
determining the critical resolved shear
stress (25).
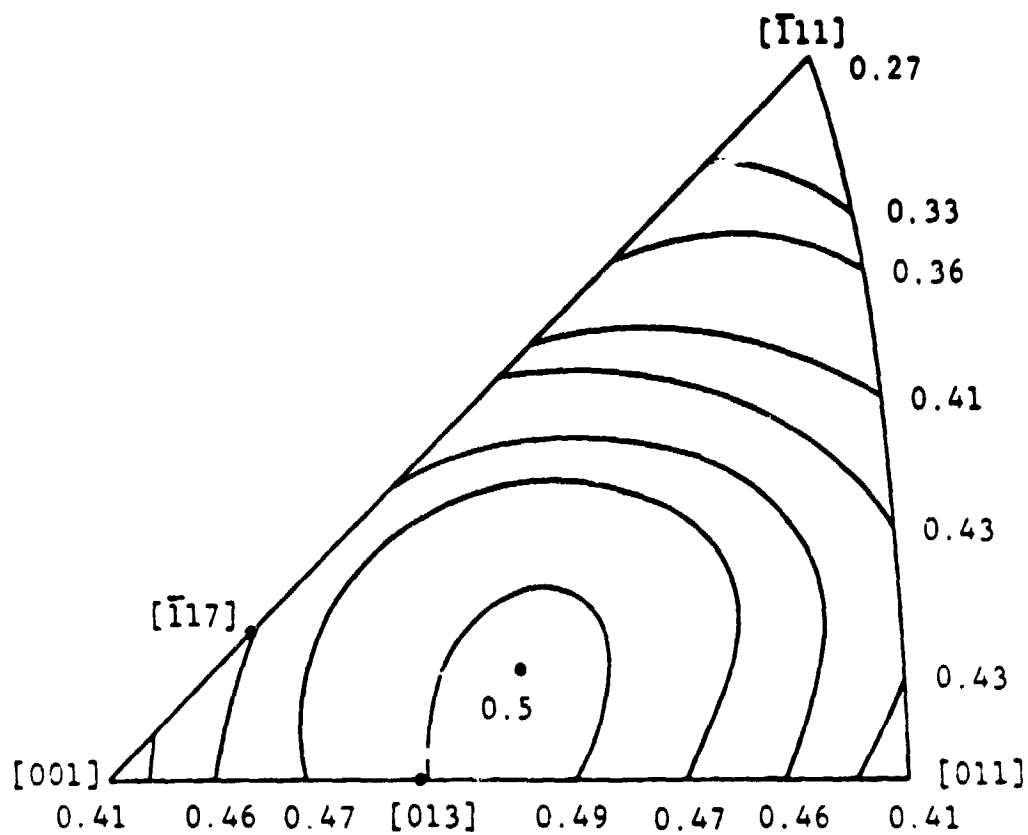
Figure 4. Schmid factor contours for the (111)[$\bar{1}$01] slip system which have been superimposed on the standard [001] - [011] - [$\bar{1}$11] stereographic triangle.
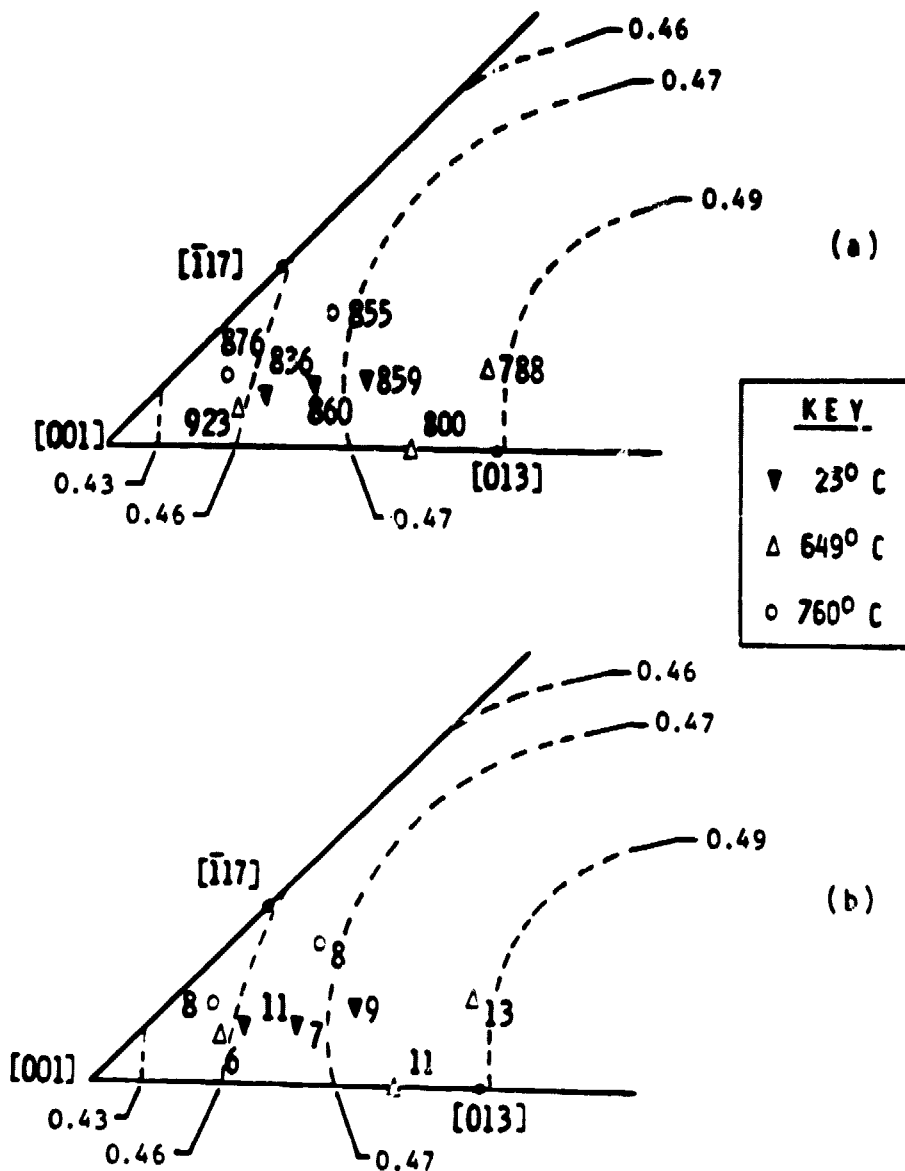
Figure 5. Portions of stereographic triangle showing the tensile behavior as a function of orientation for Mar-M247 single crystals tested at 23, 649, and 760°C (24). The numbers associated with the orientations indicate: (a) yield strength, MPa; and (b) elongation, percent.
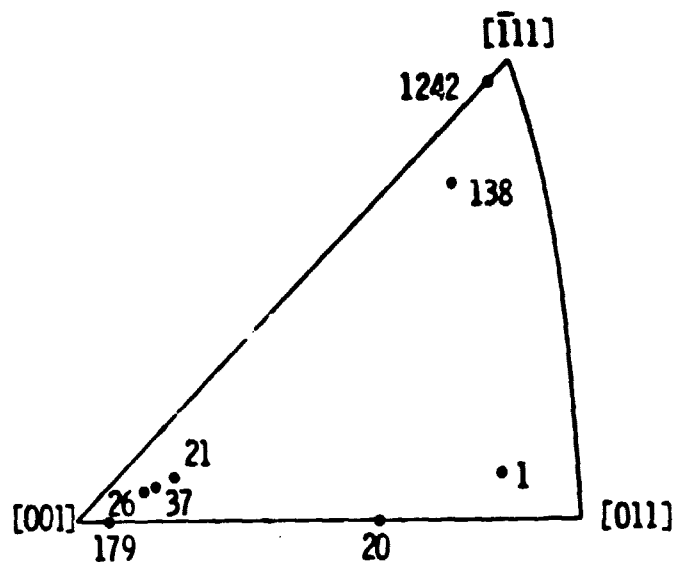
(a) 774°C, 724 MPa
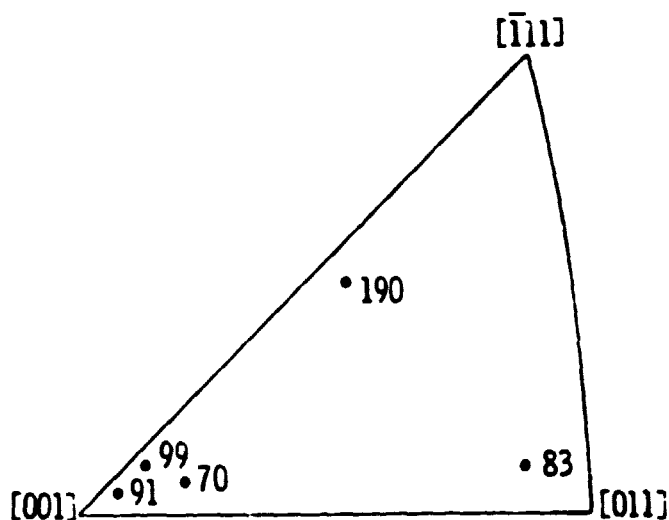
(b) 982°C, 207 MPa

Figure 6. Stress rupture lives shown as a function of
orientation for exothermically cast Mar-M247
single crystals tested under two different
conditions (24). The numbers associated with
the orientations indicate the lives in hours.
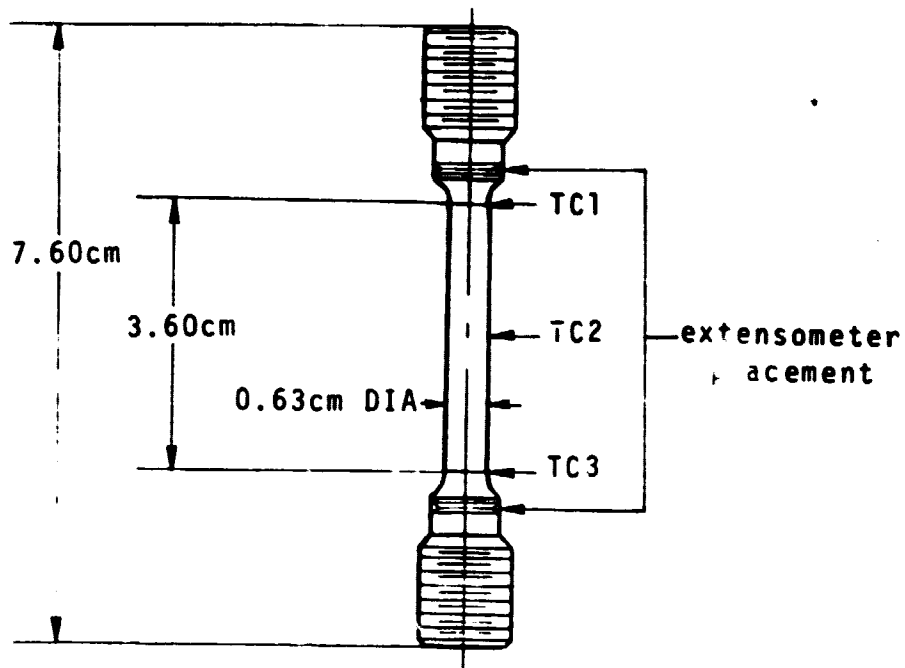
Figure 7. Specimen configuration which shows the location of the ridges in which the extensometer knife edges were placed. Location of thermocouples (TC1, TC2, TC3) is also shown.

Figure 8. Scanning electron micrograph showing the
γ - γ' eutectic (lower left corner) con-
tained in the interdendritic region of a
fully heat treated Mar-M247 single crystal.

(a)

50μ

(b)

5μ
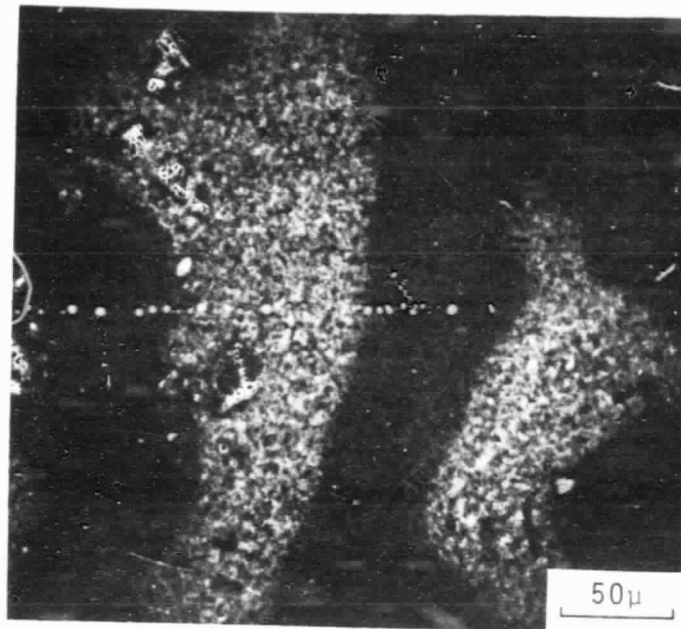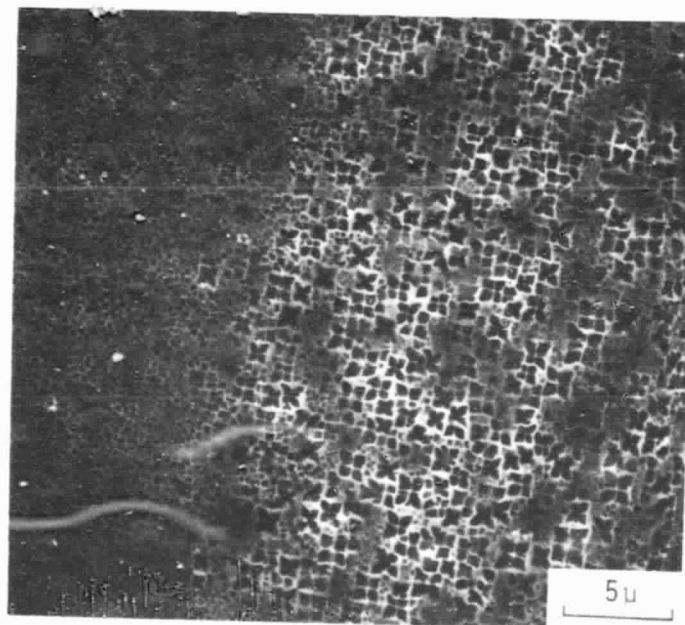
Figure 9. Scanning electron micrographs of a fully heat
treated Mar-M247 single crystal showing the
(a) coring produced during solidification,
and (b) change in γ' size at the interface
between a dendrite core and interdendritic
region.

ORIGINAL PAGE
BLACK AND WHITE PHOTOGRAPH

(a)

1μ

(b)

1μ
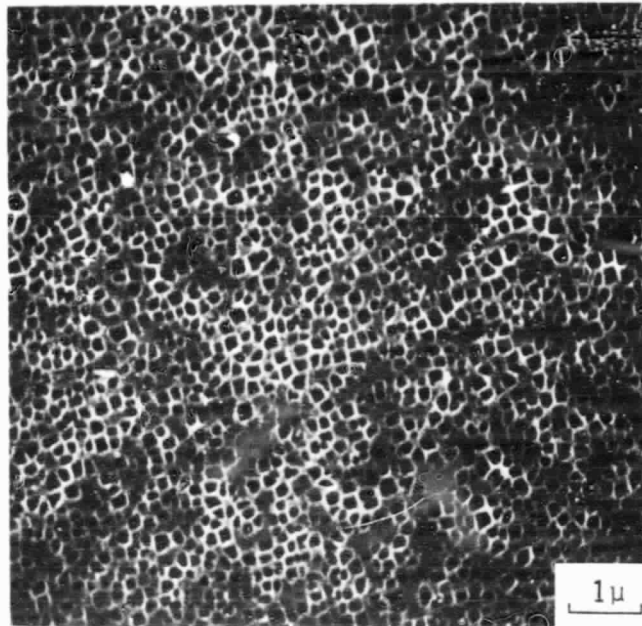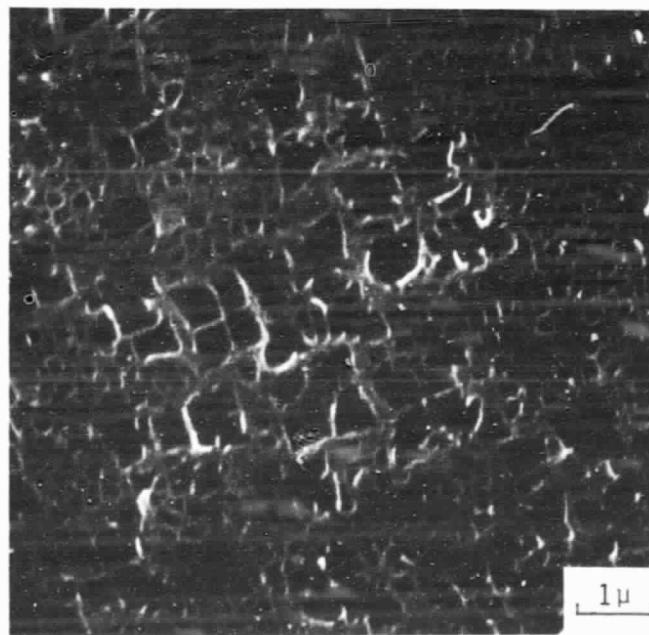
Figure 10.   Scanning electron micrographs showing the
γ' particles within the (a) dendrite centers
and (b) interdendritic regions of a fully
heat treated Mar-M247 single crystal.
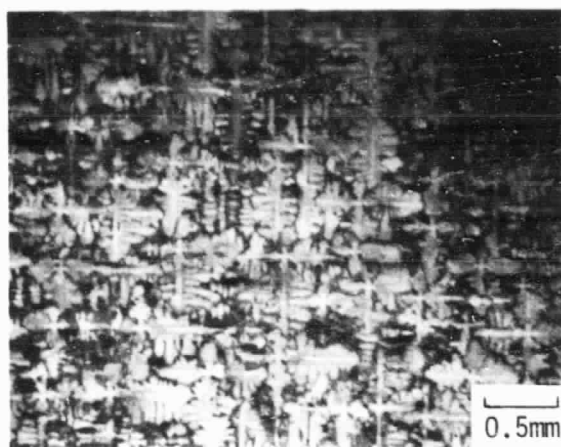
(a)   cross section
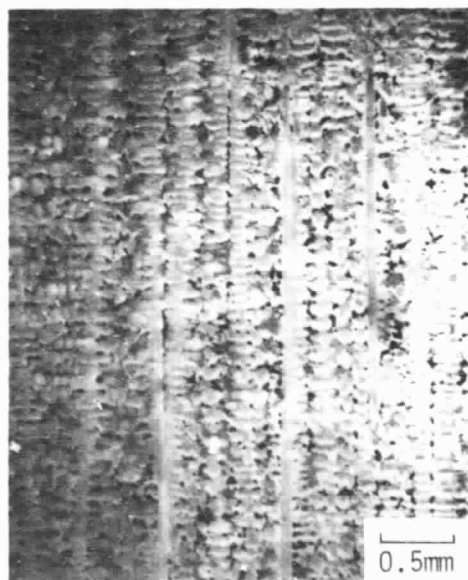
(b)   longitudinal section

Figure 11.   Macrostructure of a cube-oriented
Mar-M247 single crystal.
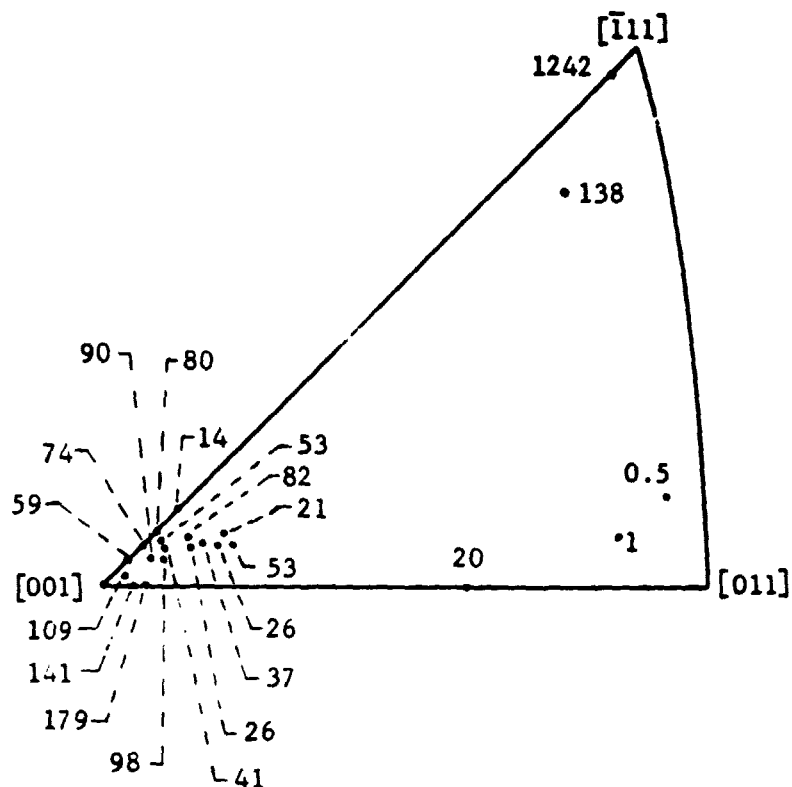
Figure 12. Stress rupture lives shown as a function of
orientation for Mar-M247 single crystals
tested at 774°C and 724 MPa. The numbers
associated with the orientations are the
lives in hours.

Figure 13. Schmid factor contours for the most highly
stressed {111}<112> slip systems. X - Y is
the dividing line between the two {111}<112>
slip systems which have the highest Schmid
factors. The (111)[112] slip system is
operative for orientations to the left of
the X - Y line; the (111)[211] slip system
is operative to the right of the X - Y line.

(a)   (b)   (c)
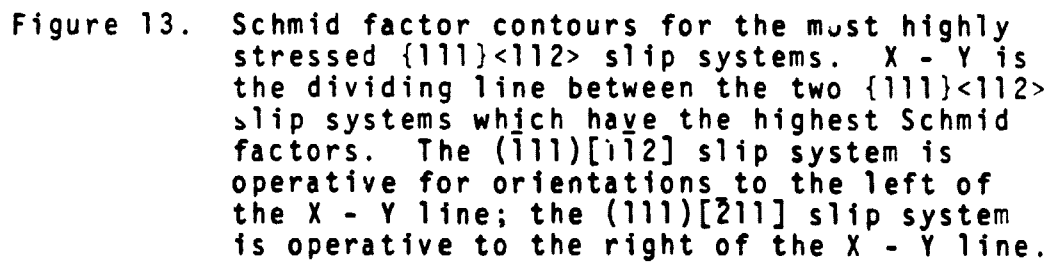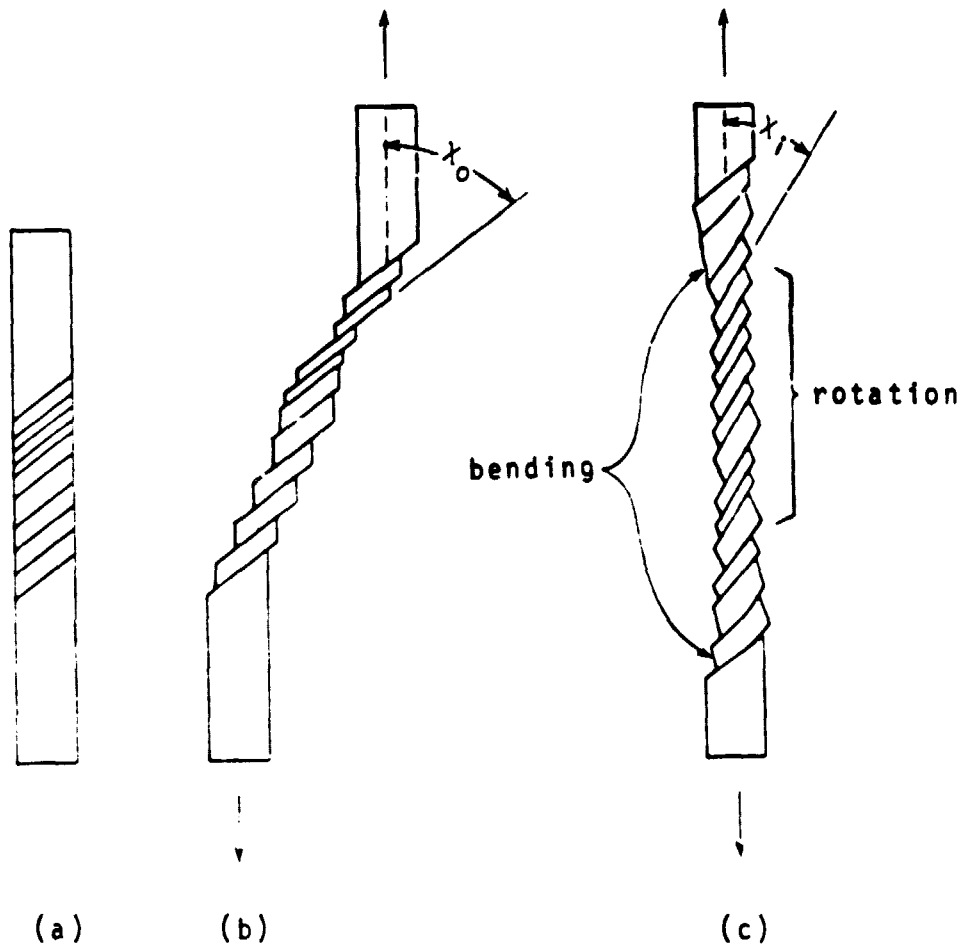
Figure 14. Schematic diagram showing the orientation of
the slip planes in a single crystal bar.
(a) Prior to deformation; (b) after deforma-
tion without grip constraint, where crystal
segments move relative to one another but
with no slip plane rotation; and (c) after
deformation with grip constraint, revealing
slip plane rotation in gage section (note
$X_i < X_o$) (41).

•[$\bar{2}$11]

[$\bar{1}$11]   •[$\bar{1}$01]   [$\bar{1}$11]

X   [$\bar{1}$12]

[001]   Y   [011]   [001]   [011]
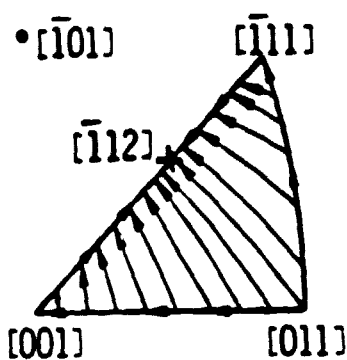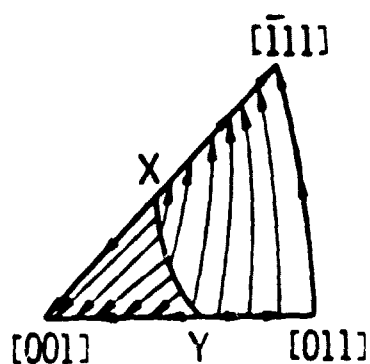
•[1$\bar{1}$2]

(a) {111}<112> slip   (b) (111)[$\bar{1}$01] slip

Figure 15.   Directions of rotation in standard stereo-
            graphic triangle for single crystals under
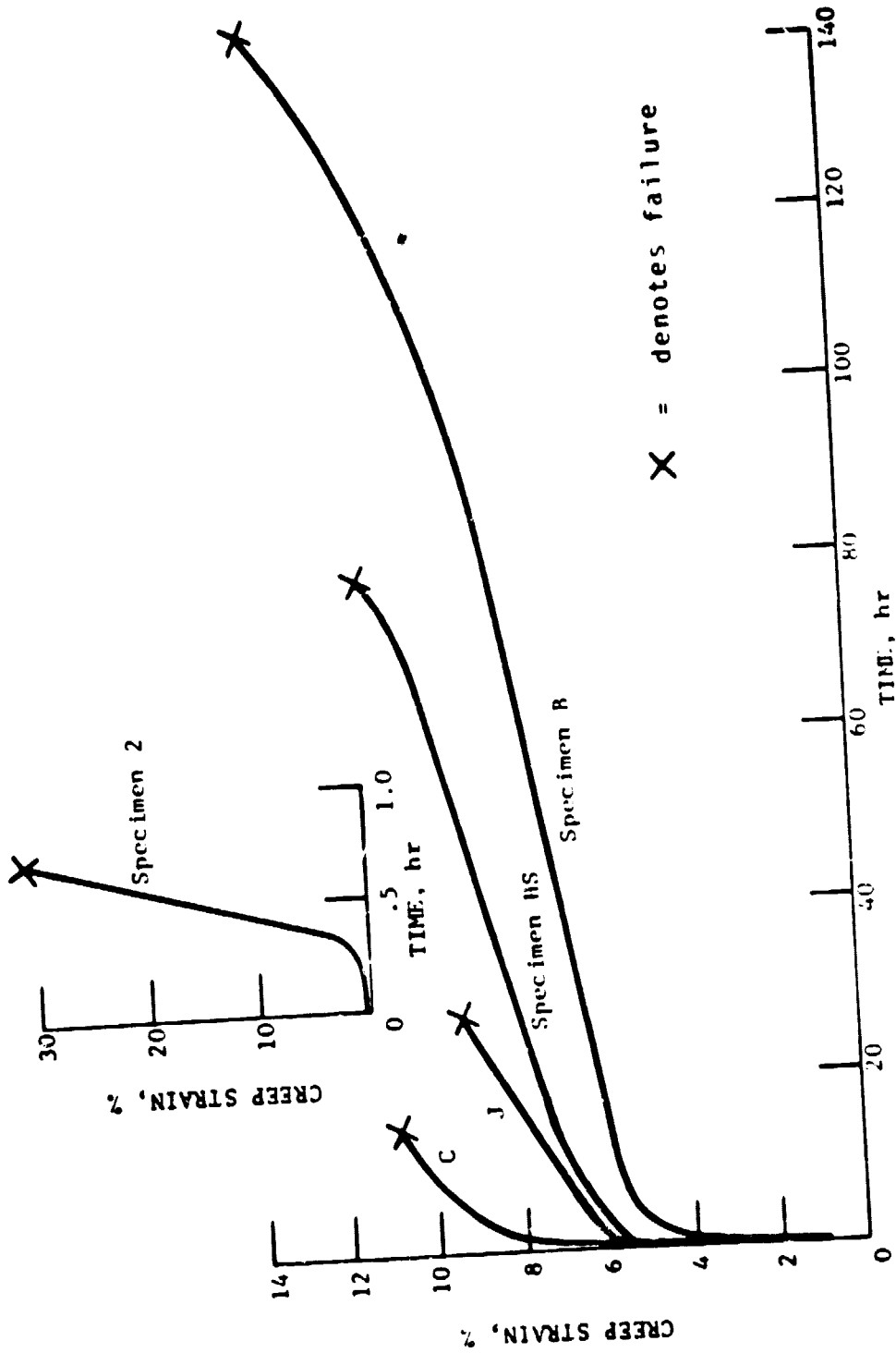   two different slip systems.

• BEFORE TESTING

x AFTER TESTING

Figure 16. Lattice rotations for selected Mar-M247
single crystals which were stress rupture
tested at 774°C and 724 MPa: (a) [001]
corner; and (b) [$\bar{1}$11] - [011] portion of
stereographic triangle. The arrows depict
the directions of rotation for the crys-
tals. The numbers associated with the
rotations represent the lives in hours.
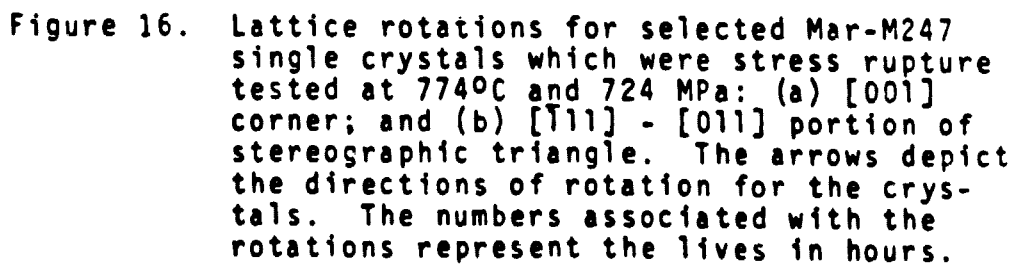
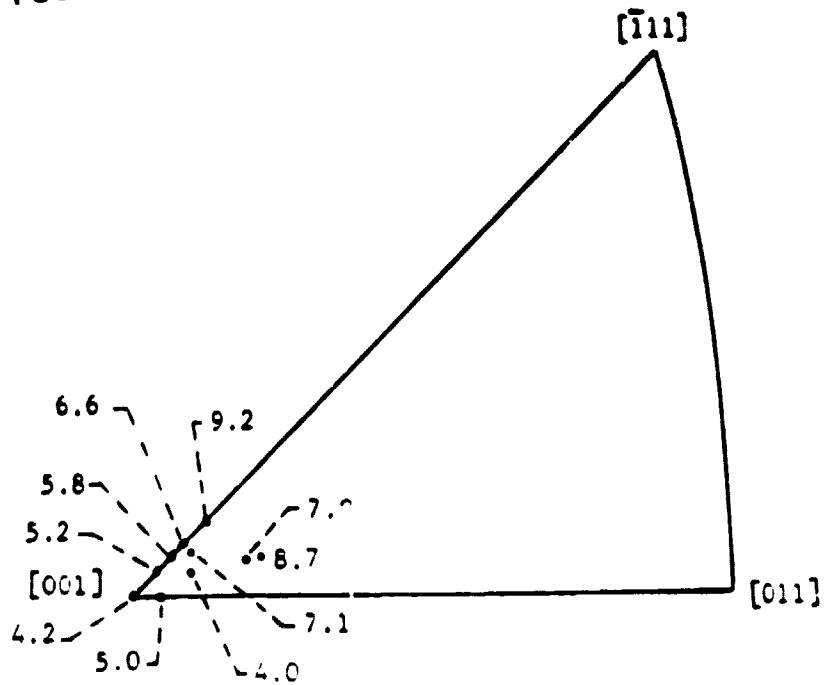Figure 17. Creep curves of selected Mar-M247 specimens tested at 774°C and 724 MPa.
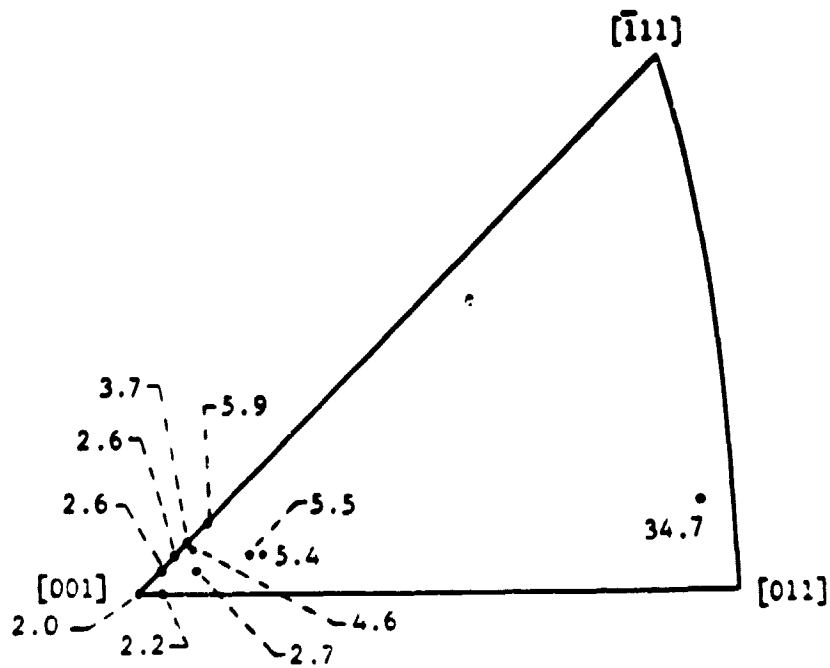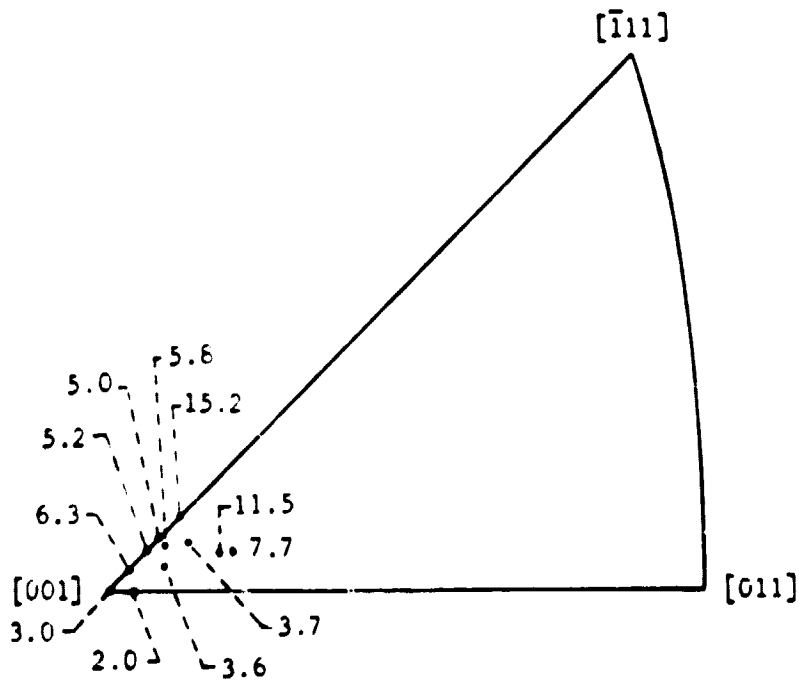
(a) Primary creep strain, ϵ_p (%)
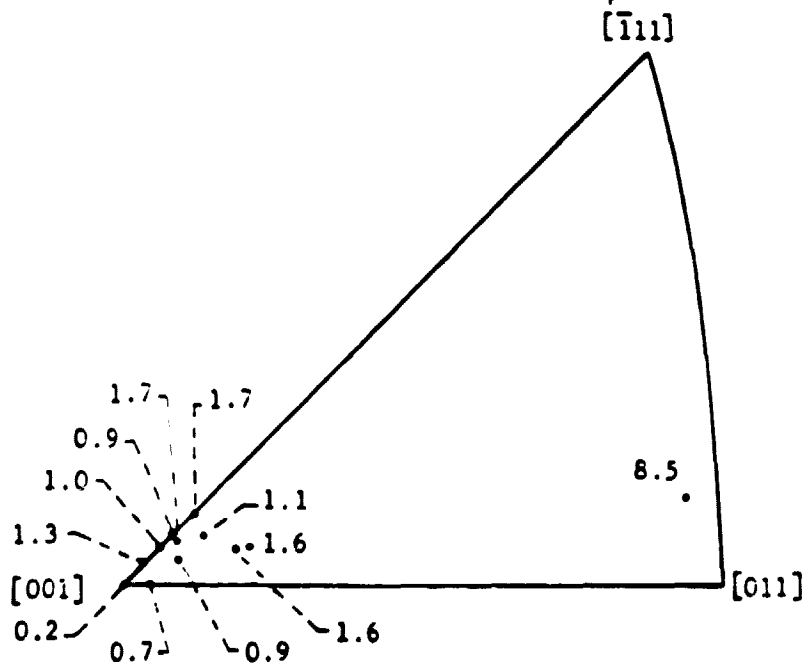
(b) Primary creep rate, $\dot{\epsilon}_p$ (x 10^{-1} hr^{-1})

Figure 18.   Creep rupture data shown as a function of
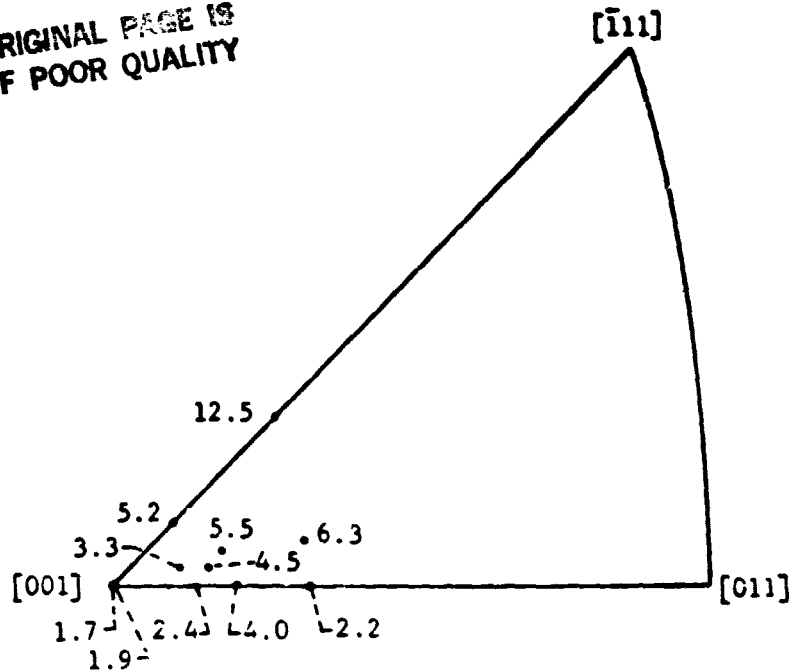orientation for Mar-M247 single crystals
tested at 774°C and 724 MPa.

(c) Strain at onset of second-stage creep, ϵ_s (%)
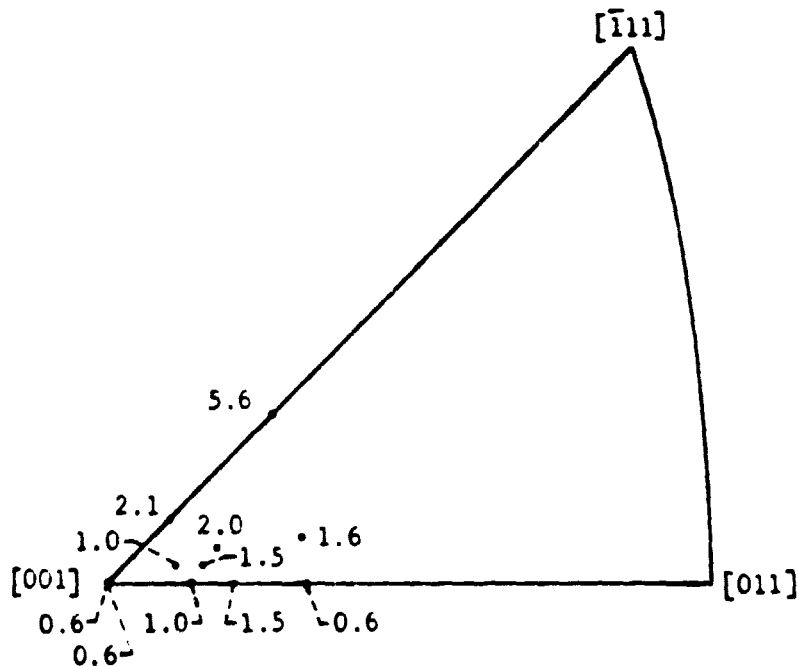

(d) Minimum creep rate, $\dot{\epsilon}_m$ (x 10^{-4} hr^{-1})

Figure 18 concluded

72

[Ī11]

12.5

5.2
3.3
5.5   •6.3
•--4.5
[001]
1.7   2.4   4.0   2.2
1.9

[011]

(a) Primary creep strain (%)

[Ī11]

5.6

2.1
1.0
2.0   •1.6
-1.5
[001]
0.6   1.0   1.5   0.6
0.6

[011]

(b) Primary creep rate (x 10^{-2} hr^{-1})

Figure 19. Mar-M200 creep data shown as a function of
orientation for sir. ie crystals tested at
760°C and 689 MPa (26).
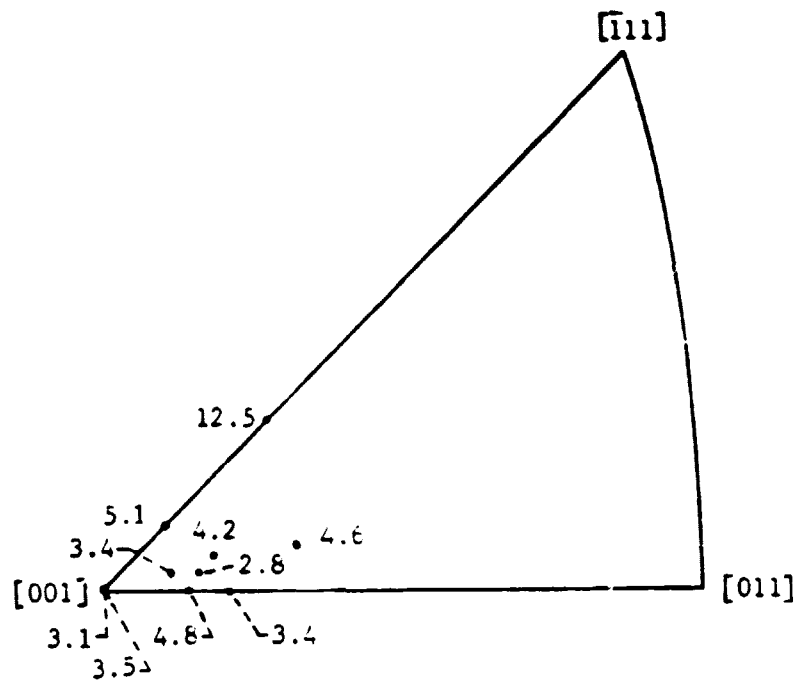
(c) Steady-state creep rate (x 10^{-4} hr^{-1})
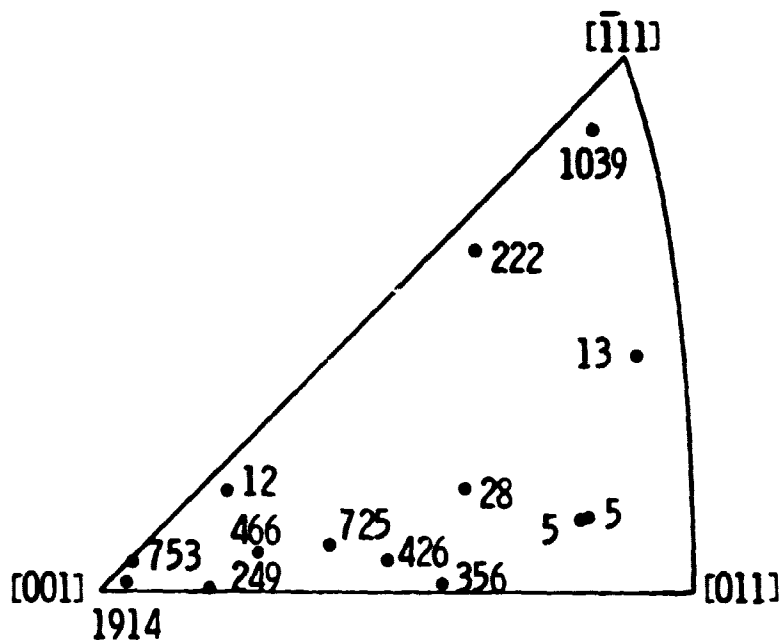
Figure 19 concluded

Figure 20.   Stress rupture lives shown as a function of
orientation for Mar-M200 single crystals
tested at 760°C and 689 MPa (10). The
numbers associated with the orientations
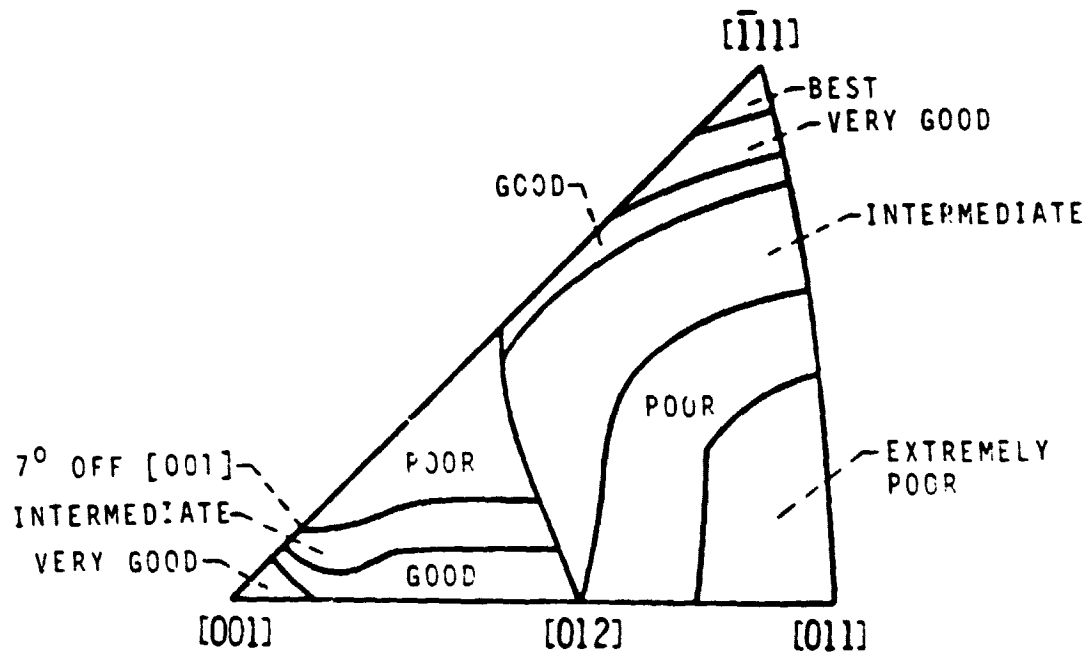are the lives in hours.

Figure 21. Suggested regimes of stress rupture lives for Mar-M247 and Mar-M200 single crystals at about 760°C.

APPENDICES

APPENDIX A

CALCULATION FOR SINGLE GLIDE IN TENSION

The amount of elongation, ϵ, necessary for a crystal gliding in single slip to rotate into a duplex slip orientation was calculated from an equation for single glide in tension (43,44):

$$\epsilon = \frac{\sin \lambda_0}{\sin \lambda} - 1 \qquad \text{(Eq. A)}$$

where λ_0 is the angle between the slip direction and the initial single slip orientation and λ is the angle between the slip direction and the duplex slip boundary orientation. The [1$\bar{1}$2] is the slip direction during first-stage creep for the Mar-M247 and Mar-M200 single crystals considered below.

Mar-M247 Single Crystal

The elongation necessary for the Mar-M247 Crystal C to reach the duplex slip [001] - X boundary was computed as follows:

$$\epsilon = \frac{\sin 43}{\sin 35} - 1$$

$$\epsilon = 18.9 \text{ \%}$$

where 43° is the angle between the [1$\bar{1}$2] and the initial orientation of the crystal; and 35° is the angle between the [$\bar{1}$1$\bar{1}$2] and the duplex slip boundary orientation. Thus, the elongation necessary for this crystal to obtain intersecting slip regions of the stereographic triangle was 18.9%. However, the elongation measured after specimen failure was only 11%. This computation provides further verification that Specimen C never reached the multiple slip [001] orientation.

Mar-M200 Single Crystal

The elongation of a 12-hour life Mar-M200 (10) single crystal is considered next in some detail. The initial orientation of this specimen is represented by the solid dot in Figure A, and the duplex slip orientation, toward which this crystal is rotating, is represented by the open circle along the [001] - [011] boundary.

The elongation necessary for this crystal to reach the duplex slip boundary was computed as follows:

$$\epsilon = \frac{\sin 47.5}{\sin 36} - 1$$

$$\epsilon = 25.4 \%$$

Thus, the elongation necessary for this crystal to obtain intersecting slip regions of the stereographic triangle was 25.4%, approximately 2.5 times larger than the 10.3% elongation (10) measured after specimen failure. It appears according to this computation that this specimen never reached the duplex slip boundary.

To calculate the position of the final orientation of this Mar-M200 specimen after creep rupture testing, the measured elongation after failure was utilized by rearranging Eq. A as follows:

$$\sin \lambda = \frac{\sin \lambda \cdot}{1 + \epsilon}$$

$$\sin \lambda = \frac{\sin 47.5}{1 + 0.103}$$

$$\sin \lambda = 0.668$$

$$\lambda = 41.9°$$

where 41.9° is the angle between the $[1\bar{1}2]$ and the calculated final orientation of the crystal. This angle corresponds to a final orientation which is 6° from the duplex slip $[001]$ - $[011]$ boundary. This calculated final orientation is represented by the x in Figure A and shows that this specimen was not able to benefit from the strengthening effects of intersecting slip. An extremely

short creep rupture life of 12 hours resulted for this
crystal.
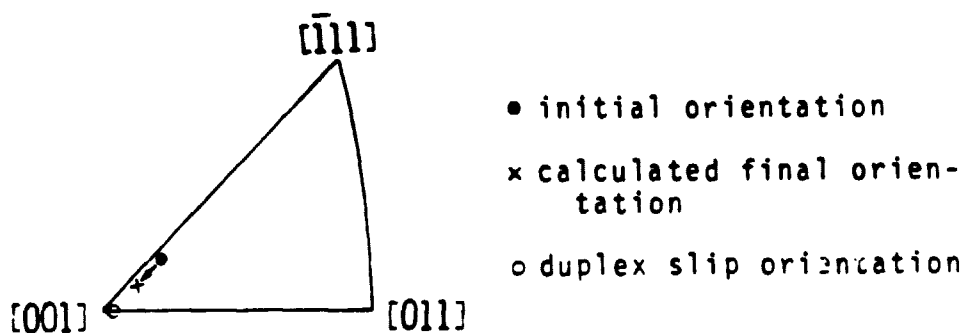
Figure A. Stereographic triangle showing the calculated
          rotation of a Mar-M200 single crystal (10)
          tested at 760°C and 689 MPa. Rupture life of
          this specimen was 12 hours.

APPENDIX B

METHODS FOR MEASURING CREEP RUPTURE DATA

The methods utilized for measuring the creep rup-
ture data of the Mar-M247 single crystals which were
tested at 774°C and 724 MPa are described below. The
definitions of ϵ_0 and t_i are illustrated in the upper
left corner of Figure B, where the initial portion of the
typical creep curve of Specimen G has been expanded to
show the appropriate detail for short-time creep. The
instantaneous strain, ϵ_0, is the elastic strain which
occurs upon initial loading of the specimen. The incuba-
tion time, t_i, is defined as the amount of time after
loading up to the point where measurable creep strain is
detected. This was taken to be the point of tangency at
which the linear primary creep region begins.

The remaining creep rates and strains obtained are
illustrated in the full creep curve of Figure B. The
primary creep rate, $\dot{\epsilon}_p$, is the slope of the linear por-
tion of the primary creep region. The primary creep
strain, ϵ_p, is defined as the total amount of strain
from ϵ_0 to the point of tangency where the primary
creep region starts to deviate from linearity. The
strain at the onset of second-stage creep, ϵ_s, corre-
sponds to the amount of strain from ϵ_0 to the point of

tangency at which the linear portion of the steady-state creep regime begins. The minimum creep rate, $\dot{\varepsilon}_m$, is the minimum slope at the onset of the steady-state creep regime.
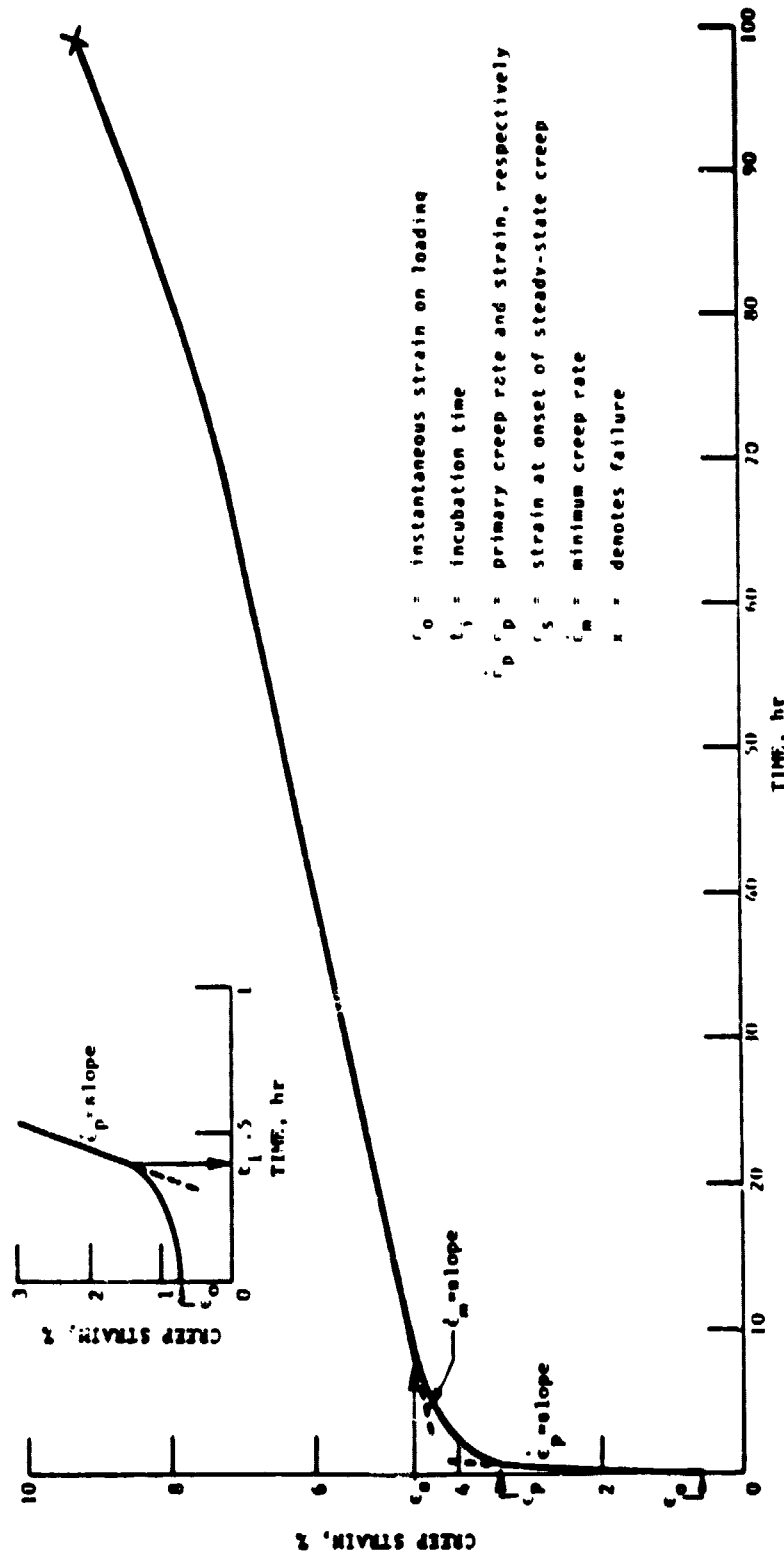
Figure B. A typical creep curve (Specimen G) for the Mar-M247 single crystals tested at 774°C and 724 MPa illustrating the definitions of the creep rupture data obtained. Short-time creep is expanded in the upper left corner.

APPENDIX C

COMPUTATION OF EFFECTIVE STRESS LEVEL
AT ONSET OF STEADY-STATE CREEP

The effective stress level, σ_e, at the onset of steady-state creep was determined as follows:

$$\sigma_e = \frac{P}{A} \qquad \text{(Eq. C - 1)}$$

where P is the load and A is the cross-sectional area at the onset of steady-state creep. Assuming constancy of volume,

$$A_o L_o = AL \qquad \text{(Eq. C - 2)}$$

where A_o is the original cross-sectional area, L_o is the original gage length, and L is the gage length at the onset of steady-state creep. The strain, e, of the specimen at the onset of second-stage creep is given by:

$$e = \frac{L}{L_o} - 1 \qquad \text{(Eq. C - 3)}$$

Rearranging and combining,

$$\sigma_e = \frac{P}{A_o} (e + 1) \qquad (Eq. C - 4)$$

where P/A_o is the nominal stress level.

The nominal stress level for the Mar-M247 single crystals tested at $774^\circ C$ was 724 MPa. The strain at the onset of steady-state creep, ϵ_s, is listed in Table III for all the Mar-M247 single crystals creep rupture tested. This strain, ϵ_s, was substituted into e in Eq. C-4. Thus, Specimen B, which had a strain at the onset of steady-state creep equal to 4.97%, was computed to have an effective stress level of 760 MPa at the onset of steady-state creep. Specimen C had a strain of 9.20% at the beginning of steady-state creep and was computed to have a significantly higher effective stress level of 790 MPa at the onset of steady-state creep.

END DATE

JAN 31, 1983